Spatial and functional arrangement of Ebola virus polymerase inside phase-separated viral factories

Jingru Fang[1,2], Guillaume Castillon[3,4], Sebastien Phan[4], Sara McArdle[1], Chitra Hariharan[1], Aiyana Adams[1], Mark H. Ellisman[4], Ashok A. Deniz[2], Erica Ollmann Saphire[1,*]

[1]La Jolla Institute for Immunology, La Jolla, CA, USA, [2]Scripps Research, La Jolla, CA, USA, [3]CMM Electron Microscopy Core facility, University of California San Diego, La Jolla, CA, USA, [4]National Center for Microscopy and Imaging Research, Center for Research in Biological Systems, University of California San Diego, La Jolla, CA, USA.

*Corresponding author (erica@lji.org)

Abstract

Ebola virus (EBOV) infection induces the formation of membrane-less, cytoplasmic compartments termed viral factories, in which multiple viral proteins gather and coordinate viral transcription, replication and assembly. Key to viral factory function is the recruitment of EBOV polymerase, a multifunctional machine that mediates transcription and replication of the viral RNA genome. We show that intracellularly reconstituted EBOV viral factories are biomolecular condensates, with composition-dependent internal exchange dynamics that likely facilitates viral replication. Within the viral factory, we found the EBOV polymerase clusters into foci. The distance between these foci increases when viral replication is enabled. In addition to the typical droplet-like viral factories, we report the formation of network-like viral factories during EBOV infection. Unlike droplet-like viral factories, network-like factories are inactive for EBOV nucleocapsid assembly. This unique view of EBOV propagation suggests a form-to-function relationship that describes how physical properties and internal structures of biomolecular condensates influence viral biogenesis.

Introduction

Viruses are architects of cellular remodeling needed to fulfill life-cycle events inside host cells. Some viruses remodel host cells by inducing formation of membrane-less compartments, also termed viral factories (VFs), that separate essential viral replication and assembly events from other cellular processes[1-11]. As exemplified by many known cellular membrane-less organelles, such as the multiphasic nucleolus[12], different cellular processes can be spatially separated into distinct co-existing phases inside the membrane-less compartment. In contrast, how multiple interdependent viral biogenesis steps are coordinated inside viral factories remains unclear.

For viruses that induce VF formation, many are non-segmented, negative-strand RNA viruses (nNSVs) [2,3,5-8,10,11]. This group of viruses include important human pathogens such as rabies virus, measles virus, respiratory syncytial virus (RSV), and Ebola virus. Inside the virion, the RNA genome of nNSVs is coated by viral nucleoprotein to form a helical RNP structure. When the virus enters a host cell, the viral genome is released into the cytoplasm and the helical RNP relaxes, which allows the viral polymerase to access and transcribe the negative-strand RNA genome into multiple mRNAs encoding individual viral genes. Viral mRNAs are translated by host cell ribosomes into viral proteins. The same viral polymerase also coordinates synthesis of a complementary strand, known as the anti-genome, which templates the replication of progeny genomes. Genome and anti-genome are immediately wrapped with nucleoprotein oligomers to form RNP-helices. However, only the genome-containing RNP (vRNP), which is linked to viral polymerase, is assembled into progeny virions[13]. The synthesis of distinct viral RNA species and sorting the corresponding viral RNA species for translation vs. assembly all happen inside the cytoplasmic space, thus likely require some spatial regulation.

Recent studies indicated that several nNSV VFs are biomolecular condensates[11,14-17] with druggable material properties that correlate with virus inhibition[18]. Biomolecular condensate formation adheres to phase separation principles where molecules divide from a mixed system into phases with distinct constituents at varying concentrations in each phase[19,20]. This process is propelled by multivalent intermolecular interactions and impacted by the physiochemical and sequence-specific characteristics of proteins (including structured and disordered regions) and RNA components[21-24]. Under physiological conditions, the concentration of key constituents essentially controls the state of intracellular phase separation, which can be approximated in a phase diagram[19]. Deciphering phase behaviors of intracellular VF condensates and the spatial localization of distinct steps of virus biogenesis within them will outline the form-to-function relationship of VFs and enhance our understanding of nNSV replication.

Among nNSVs, Ebola virus is a zoonotic, human pathogen that causes near-annual outbreaks of disease with up to 90% mortality [25,26]. The only FDA-approved vaccine for Ebola virus protects against only Ebola virus Zaire (EBOV), and not the other pathogenic species. Further, therapeutic antibodies approved thus far are also specific for EBOV and may poorly penetrate immune-privileged sites where EBOV can lurk. Additional therapeutic strategies are needed, and will be accelerated by a better understanding of essential mechanisms in EBOV replication.

A hallmark of EBOV infection is the formation of eosinophilic, cytoplasmic inclusion bodies[27], which we now refer to as viral factories (VFs). EBOV nucleoprotein (NP) is considered the building block of VFs: in infected cells, VFs always contain NP, and in transfected cells, entropically expressed NP can induce VF-like, cytoplasmic granules. VFs recruit EBOV large polymerase protein L, polymerase cofactor VP35, and transcription factor VP30[28] through NP-VP35[29,30], L-VP35[31] and NP-VP30[32] interactions. Recruitment of L, VP35 and VP30 to EBOV VFs transform VFs into sites for active replication and transcription of viral RNA genome[6]. Further recruitment of EBOV minor matrix protein VP24 to VFs through NP-VP24 interaction[33] triggers the assembly of viral nucleocapsid. Given the biosafety level-4 requirement to work with live EBOV, reconstitution[29] and reverse genetic systems[33-35] have become routine practices to study molecular mechanisms underlining EBOV replication, transcription, and assembly or EBOV VFs formation. It is unclear whether the morphology, dynamics and internal forces of the VF condensates correlate with the coordination of EBOV biogenesis events.

Here, we define the spatial regulation of viral RNA synthesis and the EBOV polymerase within intracellular viral factories. We determine that reconstituted EBOV VFs exist as biomolecular condensates and dissect the contribution of key viral proteins to intracellular VF phase behaviors. Using multi-scale imaging approaches, we provide an unprecedented view of the spatial organization by which Ebola virus orchestrates multiple biogenesis steps and deploys viral replication machinery inside viral factories.

Results

1. An mNeonGreen-tagged EBOV VP35 can be used for live cell imaging of reconstituted viral factories (VFs)

Intracellular EBOV VFs are found to undergo fusion during infection[6]. This observation served as the first hint that EBOV VFs could be biomolecular condensates. Thus, we undertook a quantitative approach to determine whether EBOV VFs are indeed fluid condensates and define the internal molecular dynamics within EBOV VFs. Since microscopy of live, EBOV-infected cells under biosafety level-4 containment is neither feasible nor amenable to controlling VF composition, we first established a transfection-based, live-cell system to perform fluorescence recovery after photobleaching (FRAP) analysis with intracellularly reconstituted EBOV VFs.

To monitor EBOV VF with live-cell imaging, we adapted an approach used to image VFs in live cells infected with Rabies[15]. We fused an EBOV VF constituent, the polymerase cofactor VP35, to an N-terminal hemagglutinin (HA) epitope tag and a fluorescent protein, mNeonGreen (mNG) to generate HA-mNG-VP35. We chose to tag EBOV VP35 instead of another VF

constituent, EBOV NP, because fluorescence-tagging of NP can ablate the biological function of NP in supporting viral RNA synthesis [36]. We confirmed that HA-mNG-VP35 expresses at a similar level as the wild-type (VP35-WT), and retains sufficient ability to act as the polymerase cofactor that supports EBOV viral RNA synthesis (**Supplementary Figure 1a**).

VP35 interacts with EBOV nucleoprotein (NP) and chaperones the NP monomer (NP^0) prior to NP oligomerization[30]. As the polymerase cofactor, VP35 bridges the EBOV large polymerase protein (L) to NP-coated viral genome[28]. Since these multivalent intermolecular interactions VP35 involved in might provide the foundation for phase separation, we first performed co-immunoprecipitations and confirmed that the mNG tag on VP35 did not affect these interactions (**Figure 1a**). Immunofluorescence microscopy showed that the intracellular localization of HA-mNG-VP35 resembles VP35-WT, when co-expressed with NP and L (**Supplementary Figure 1b**). Together, our results indicate that HA-mNG-VP35 preserves sufficient polymerase-cofactor function and fully retains interactions with NP and L for use in live-cell imaging.

2. Reconstituted EBOV VFs display composition-dependent, phase separation behaviors in live cells

To measure the internal exchange of EBOV VF components in a cellular context, we performed FRAP in HEK 293T cells co-transfected with EBOV NP and HA-mNG-VP35. Both NP and VP35 proteins contain intrinsically disordered and low complexity regions (**Figure 1b**), bind RNA[37,38], and self-oligomerize[39-42], all common features associated with known cellular proteins to be involved in phase separation[19]. Here we used NP and VP35 as the minimal components to reconstitute EBOV VFs. Reconstituted EBOV VFs had diameters ranging from sub-micrometer to 10 μm (**Supplementary Figure 1c**). Because the high mobility of sub-μm VF prevents accurate measurement and quantification of fluorescence recovery, we focused on medium-sized VFs (4-5 μm diameter) and photobleached a center spot within these sizable VFs (**Methods**).

As a control, HA-mNG-VP35 expressed alone phase separated in the cytoplasm (**Figure 1c**). Most cells have large quantities of small (sub-μm) VP35-containing dense phases (condensates) with high apparent mobility relative to the dilute phase, but a small number of condensates had a larger size suitable for FRAP. These large condensates have multiple internal regions lacking fluorescence, which coincides with a “sponge-like” phenotype of VP35-condensates in a previous electron microscopy study[43]. Within these VP35-condensates, we observed slow internal molecular exchange (**Figure 1f,** green curve), which could be mediated by VP35 self-oligomerization[41,42] or heterotypic interactions between VP35 and endogenous dsRNA[44,45], since diffusion of a similar-sized protein across a cytoplasmic spot (a circle with 2 μm diameter) occurs within milliseconds[46].

We next evaluated reconstituted EBOV VFs via co-expression of HA-mNG-VP35 and NP. The combination of HA-mNG-VP35 and NP yielded binary condensates (**Figure 1d**) that appeared to be fluid-like based on frequently observed fusions between condensates or fission of one condensate into two parts (**Supplementary Figure 2a**), and on non-fluorescence objects trafficking through VFs (**Supplementary Figure 2b**). Over half the transfected cells had easily identifiable >5 μm condensates. Fluorescence recovery of VP35-NP condensates is more complete (mobile fraction ~85%) than that measured in VP35-alone condensate (mobile fraction < 50%) (**Figure 1f,** red vs. green curves). This result indicates that the VP35-NP interaction can mobilize molecules inside VF condensates. We also noticed the kinetics of internal molecular exchange measured with Ebola VP35-NP condensates ($t_{1/2FAST}$ ~5.5 s) is similar with that reported for VFs in rabies virus infected cells[15] ($t_{1/2FAST}$ ~5.2 s) (**Figure 1f**).

Co-expression of mNG-HA-VP35 with NP and EBOV large polymerase protein (L) resulted in dense phases in the cytoplasm that contained all three proteins (**Figure 1e, Supplementary Figure 1b**). In VP35-NP-L condensates, the mobile fraction of mNG-HA-VP35 (**Figure 1f**, blue curve) is on average 7% lower than VP35+NP binary condensates and the percentage of molecules participating in fast association event (%fast) is on average 16% lower than binary

condensates. This result suggested that VP35-L interactions could immobilize a small population of VP35. In both binary and ternary condensates, bleach pulses induced loss of fluorescence signal to around 12% of the prebleach signal at equilibrium (**Supplementary Figure 2c**). Further, the similar kinetics ($t_{1/2}$) for binary and ternary condensates likely indicates similar modes of molecular interactions are driving the VP35 mobility (**Figure 1f**).

With the same composition of binary EBOV VFs, we next evaluated the contribution of an intrinsically disordered region (IDR) in EBOV NP to the internal exchange dynamics within VFs. Although EBOV VP35 also contains an IDR, which spans the first 80 residues on the N terminus (**Figure 1b**), this region mediates the binding of VP35 to NP^0, and is thus too important to be removed for a deletion mutant[30]. In contrast, deletion of NP IDR (a.a. 500-739) partially preserves NP-VP35 interaction and recruitment of VP35 to NP-induced VFs[29]. We made a corresponding deletion mutant of NP, termed NPΔ (500-739), and co-expressed it with mNG-HA-VP35 (**Supplementary Figure 3a**). However, the internal exchange dynamics of NPΔ (500-739)-VP35 binary condensates were similar to NP-VP35 condensates (**Supplementary Figure 3b, c**), which means the IDR in EBOV NP is dispensable for controlling the internal exchange of binary VFs.

Our FRAP results quantitatively showed that EBOV VFs reconstituted with NP and VP35 display composition-dependent, internal exchange dynamics in live cells. The addition of L immobilizes a small, but detectable, fraction of VP35 inside the reconstituted VFs.

3. FLAG-tagged EBOV large polymerase protein L forms foci inside EBOV VFs

We next assessed whether EBOV L is immobilized in a specific location within VFs using immunofluorescence microscopy. To facilitate detection of L, we engineered recombinant L with an N-terminal 2xFLAG tag (FLAG-L) as previously described[31] since the only currently available L polyclonal antibody can non-specifically bind to proteins other than EBOV L (**Supplementary Figure 1d**).

First, we co-expressed NP, VP35 and FLAG-L in HEK 293T cells and labeled EBOV VFs using a monoclonal antibody targeting NP. Although NP was present throughout EBOV VFs, NP molecules at the VF periphery were immunolabeled more efficiently than the NP inside VF, leading to an “empty” droplet-like morphology of EBOV VFs, which was previously described[47,48]. We reasoned that this preferential immunolabeling of periphery NP could be due to the more expanded conformation of NP molecules and fewer intermolecular interactions located at the VF periphery than the interior[49]. Unexpectedly, FLAG-L was not homogenously distributed within reconstituted VFs and had a different staining pattern than NP (**Figure 2a**). Instead, FLAG-L clustered into networks comprising interconnected foci within the ternary condensate, suggesting that an intrinsic property of L drives a different phase behavior than VP35 or NP.

To link this phase behavior of EBOV L to its biological function, we further analyzed L localization in the presence of an active RNA substrate for L, the EBOV minigenome (MG), which allows recapitulation of L-mediated replication and transcription. The EBOV MG we used here is bicistronic (2cis-MG), which contains two reporter genes encoding GFP (for imaging) and *Renilla* luciferase (for quantification) in a tandem cassette carrying authentic EBOV gene start- and end signals. EBOV regulatory sequences, the 3' leader and 5' trailer, required for replication, transcription and encapsidation of viral RNAs[50], flank the bicistronic cassette. Using the replication-competent version of the 2cis-MG (**Figure 2b**, Rep-comp. MG), we confirmed that the L construct, FLAG-L, we engineered is competent to fulfill its biological function as it retained 74% of the wildtype L (L-WT) activity (**Figure 2c**).

In GFP-positive cells having successful reconstitution of EBOV MG replication and transcription, FLAG-L still clustered into networks of interconnected foci inside VFs (**Figure 2d**). For comparison purposes, we chose not to consider the FLAG-L localization in GFP-negative cells, as expression of any EBOV protein or MG RNA might be lacking in these cells. Further, we noticed that due to chemical fixation, GFP reporter signals were preferentially trapped in both VFs and nucleoli in fixed cells.

202 We next asked whether modulating viral RNA synthesis affects the organization of EBOV L
203 polymerase inside VFs. Since adding or removing MG system elements could affect the overall
204 valency of protein-protein/RNA interactions or the molecular composition inside EBOV VFs, we
205 incorporated a previously characterized mutation into the 5' trailer of the EBOV 2cis-MG that
206 allows transcription, but disables genome replication[51]. Reporter activity measured in this
207 replication-deficient MG (Rep-def. MG) system reflects only viral transcription (**Figure 2b**, Rep-
208 def. MG). With Rep-def. MG, FLAG-L retained 33% of the L-WT activity, indicating that the
209 2xFLAG tag may have affected L-mediated transcription (**Figure 2c**). Nevertheless, with FLAG-
210 L, when replication was disabled, the L foci inside EBOV VFs were more closely spaced compared
211 to that seen for replication-competent VFs (**Figure 2e, f**). This different spacing is unlikely to be
212 associated with the expression levels since FLAG-L was expressed at equivalent levels in the
213 Rep-comp. and Rep-def. MG systems (**Figure 2c**). Together, our results revealed a unique
214 localization pattern of EBOV polymerase L inside VF and established a potential link between the
215 spatial distribution of L within the VF and viral RNA synthesis events mediated by L.

216 **4. Network-like VFs exist in EBOV-GFP-ΔVP30 infected cells**

217 Among the EBOV VFs reconstituted with the transcription and replication of EBOV MG in
218 transfected HEK 293T cells, some display a granular, network-like morphology instead of the
219 typical droplet-like morphology (**Figure 3a**). We thus examined whether network-like VFs also
220 occur during virus infection.

221 To characterize VF morphology in EBOV-infected cells, we used the biologically contained
222 EBOV-GFP-ΔVP30 virus, which is morphologically indistinguishable from wild-type EBOV but
223 approved for use in biosafety level 2+ containment[52]. In this system, a GFP gene replaces the
224 gene encoding the viral transcription factor, VP30, so that EBOV-GFP-ΔVP30 virus can grow only
225 in cell lines stably expressing VP30. Here, we infected Vero cells stably expressing EBOV VP30
226 (Vero-VP30) with EBOV-GFP-ΔVP30 in a synchronized manner, and we fixed and inactivated
227 these cells at 18 hours post-infection. We chose this time point because levels of viral proteins
228 and GFP reporters are above the detection threshold, and the VF size is comparable to that in
229 HEK 293T cells transfected with the EBOV MG system[53]. We then used immunofluorescence-
230 labeled NP as a marker to detect VFs in GFP-positive (i.e., EBOV-GFP-ΔVP30 infected) Vero-
231 VP30 cells.

232 EBOV-GFP-ΔVP30 infected cells had either droplet-like or network-like VFs (**Figure 3b**), with
233 the majority (77%) having droplet-like VFs and a stronger immunofluorescence staining of NP at
234 the VF periphery, as previously reported[53]. The remaining 23% of infected cells harbored network-
235 like VFs, which, in contrast to droplet-like VFs located at discrete sites in the cytoplasm, occupied
236 a more extended region that included a group of small, granular VFs either interconnected or
237 separated by only a tiny distance. This network-like phenotype could reflect a later stage of EBOV
238 life cycle when helical viral RNPs are assembled into filamentous nucleocapsids about 1 μm in
239 length[54,55] and depart from VFs (**Supplementary Figure 4**). The departure of assembled viral
240 nucleocapsids can disintegrate VFs. However, we did not identify any assembled nucleocapsids
241 nearby these network-like VFs (**Figure 3c, d, e**), suggesting that these network-like VFs are not
242 the immediate source of EBOV nucleocapsid assembly.

243 To understand why network-like VFs cannot support EBOV nucleocapsid assembly, we
244 analyzed whether building blocks of viral nucleocapsids[56], which include EBOV NP, VP35, VP30,
245 and VP24, are present in network-like VFs. We found network-like VFs contain EBOV NP and
246 VP35 (**Figure 3c**), a low level of VP30 (**Figure 3d**), but not VP24 (**Figure 3e**), which is necessary
247 for nucleocapsid assembly[57]. Our results indicated that both the droplet-like and network-like
248 morphology of EBOV VFs exist during EBOV infection. Given the expression of the GFP reporter,
249 which is encoded in the viral genome, both types of VFs support EBOV gene expression, but only
250 the droplet-like VFs support viral nucleocapsid assembly.

5. Engineering a split-APEX2 tag for electron microscopy analyses of EBOV polymerase L-VP35 complexes

To dissect the spatial organization of EBOV polymerase inside VFs at nanometer resolution, we used APEX2, a peroxidase tag engineered to indicate the location of tagged proteins in electron microscopy (EM) imaging. Specifically, we used the split-APEX2 (sAPEX) tag[58], consisting of two inactive fragments, sAP and sEX. We genetically fused the small fragment sEX to L (L-sEX) and the large fragment sAP, along with a V5 epitope tag, to VP35 (VP35-V5-sAP) (**Figure 4a**). Interaction of L with VP35 during the formation of an active EBOV polymerase complex joins the sAP and sEX fragments to reconstitute APEX2 peroxidase activity.

We confirmed that sAPEX-tagged EBOV polymerase is functionally active, using a Pol1-based, monocistronic EBOV minigenome (Pol1-MG) system[35] that works similarly to the T7-based, bicistronic EBOV MG, but contains a single, firefly luciferase reporter gene (**Figure 4b, c**). VP35-V5-sAP expression levels were significantly higher than the V5-tagged VP35 control (VP35-V5). L-sEX was also expressed to higher levels than wild type L (**Figure 4d**), suggesting the additional interaction provided by sAPEX could stabilize both L and VP35 proteins. In cells transfected with sAPEX2-tagged EBOV polymerase and the Pol1-MG system, we confirmed a site-specific reconstitution of sAPEX2 activity, as evidenced by APEX2-mediated conversion of a fluorogenic substrate at sites marked with VP35-V5-sAP immunofluorescence.

We noted that VP35-V5-sAP formed a network-like dense phase, whereas VP35-V5 formed droplet-like dense phases (**Figure 4e,** L-WT + VP35-V5). These two morphologies of VP35-dense phase in transfected HEK293T cells are similar to those we observed with EBOV VF in infected cells, although network-like VFs in transfected cells showed higher connectivity than in virus-infected cells. We reasoned that network-like morphology of VP35-V5-sAP could be related to increased valence of the inter-molecular interaction in the sAPEX2-tagged L-VP35 complex, since trans-complementation of the sAPEX-tag creates an additional intermolecular interaction between L and VP35 (**Figure 4e,** L-VP35-sAPEX2). To test this possibility independently of sAPEX2-tagging, we increased the valence of inter-molecular interactions that involve VP35 by adding VP24, an EBOV protein which also interacts with VP35[33]. Upon co-expression of VP24 with VP35-V5 and the Pol1-MG system, VP35-V5 droplets were replaced by the highly-connective, network-like VP35-V5 dense phase that colocalized with VP24 (**Figure 4f**, L-WT + VP35-V5). This result indicates that increased valence of intermolecular interactions indeed alters VP35 phase behavior. Even in the presence of VP24, the sAPEX2-tagged EBOV L-VP35 complex remained in the network-like dense phase (**Figure 4f**, L-VP35-sAPEX2).

In summary, we successfully engineered an intracellularly active EBOV polymerase carrying a split-APEX2 tag that will allow localization of EBOV polymerase in electron microscopy (EM) analyses. Although the split-APEX2 tag did change the intracellular localization pattern of VP35 from droplets to networks, we have observed similar network-like VFs in EBOV-GFP-ΔVP30 infected cells. Therefore, we next carried out EM analysis on the localization of sAPEX2-tagged EBOV polymerase in cells reconstituted with the EBOV MG system.

6. Nanoscale localization of split-APEX2-tagged EBOV polymerase complex with thin-section transmission electron microscopy (thin-section TEM)

We used the sAPEX2 tag engineered into the L-VP35 complex to locate the EBOV polymerase within the compact cellular contents revealed by EM. Upon staining with 3,3′-diaminobenzidine (DAB), trans-complementation of sAPEX2 catalyzes DAB polymerization with minimal diffusion. The resulting DAB polymers alone at the site of active APEX2 are chromogenic, which can be detected by light microscopy. Further, DAB polymers are osmiophilic, and thus capture osmium upon OsO_4 staining to increase electron density associated with DAB deposits (**Figure 5a**). OsO_4 also stains unsaturated lipids[59] and reacts with nucleic acids[60,61] to outline cellular architecture in a specimen.

After optimization of transfection and staining conditions, we could detect sAPEX2-specific DAB deposits in bright field light microscopy images of HEK 293T cells transfected with sAPEX2-tagged EBOV polymerase together with other Pol1-MG components. DAB darkening was intensified after osmification and DAB-positive (DAB+) cells were readily recognizable in resin-embedded samples under light microscopy, which facilitates production of 70 nm thin-sections containing a DAB+ cell and its detection with transmission electron microscopy (TEM) (**Figure 5b**). We observed within the same DAB+ cell network-like, electron-dense regions in cytoplasmic areas that likely correspond to EBOV VFs (**Figure 5c, Supplementary Figure 5a**). These electron-dense regions were present in cells transfected with the Pol1-MG system but not in untransfected control cells (**Supplementary Figure 5b, c**). In the DAB+ cell, EBOV-specific electron-dense regions were decorated with darker dots arranged in a pattern that correlated with the shape of DAB darkening in light microscopy (**Figure 5c,** arrows), suggesting that the locations of these darker dots in the electron micrograph corresponded to sites where sAPEX2-tagged EBOV polymerases localize.

In the same thin-section, we also identified cells that had no DAB staining under light microscopy (DAB-) (**Figure 5b**). These DAB- cells had the same transfection conditions as DAB+ cells, but sAPEX2 activity was not reconstituted. DAB- cells exhibited network-like, electron-dense VFs in the cytoplasm, similar to DAB+ cells (**Figure 5d**). By comparing the morphology of EBOV VF in DAB+ and DAB- cells, the darker dots that associate with electron-dense VF in the DAB+ cell in fact indicate locations of sAPEX2-tagged EBOV polymerase (**Figure 5e**).

Our thin-section TEM observation revealed that sAPEX2-tagged EBOV polymerase non-uniformly localizes to the periphery of network-like VFs. In several sites in the cytoplasm, sAPEX2-tagged EBOV polymerase preferentially clusters at the junction of interconnected VFs. Surrounding the electron-dense VFs were wire-like fragments that frequently associated with neighboring VFs (**Figure 5c, d**).

7. sAPEX2-tagged EBOV polymerase complex locate at the periphery or interconnected spots of network-like VFs

To visualize the three-dimensional (3D) ultrastructure of EBOV VFs and elucidate the spatial distribution of the sAPEX2-tagged polymerase complex, we applied electron tomography (ET) and reconstructed tomograms of subcellular volumes containing EBOV VFs and sAPEX2-tagged polymerase. Thin-section TEM allowed visualization of averaged 2D projection of all cellular content across the thin-section specimen, but multi-tilt electron tomography allowed us to resolve individual tomographic slices of the reconstructed volume with finer details of cellular matter (**Figure 6a, Supplementary Movie 1**). Similar to previous EM analysis of virus-infected cells[3,62], reconstituted EBOV VFs appeared as electron-dense clusters that lack membrane boundaries themselves, but are in close proximity to membrane-bound cellular organelles including mitochondria, the endoplasmic reticulum, the nuclear envelope and vesicles.

Across the tomographic slices, darker-stained patches near the edge of several electron-dense VFs were apparent. By mapping these darker patches in the tomogram, we reconstructed the 3D footprints of sAPEX2-tagged EBOV polymerase on a group of network-like VFs that were in close proximity or even interconnected (**Figure 6b, Supplementary Movie 1**). We then selected a region of interest from the whole tomogram, and performed a finer manual segmentation focusing on smaller objects surrounding the VFs (**Figure 6c**). sAPEX2-tagged EBOV polymerase appeared to dock at certain spots on the VF periphery. Ribosomes were located outside, but adjacent to EBOV VFs. We observed several loosely coiled structures either emerging from or passing through neighboring VFs, which likely gave rise to the rough surface of the VFs and are the major component of VFs (**Figure 6d**). We propose that these loosely coiled structures are the viral RNP (vRNP), which has at its core helical viral genomic RNA bound to NP[55,63]. The helical structure is sufficiently relaxed to allow the viral polymerase to slide along the

349 genome during RNA synthesis. We saw no condensed vRNP in our sample, likely because VP24,
350 which is essential for condensing vRNP, was not included in the current MG system[64,65].
351 In a selected region from the whole tomogram, two loose-coil structures can, in fact, be traced
352 back from their different branching sites to one parental loose coil (**Figure 6e**). One possible
353 explanation for these interconnected coils is that viral genomic RNA associates with active
354 transcription products. For several better-resolved loose coils in our tomogram, the coil terminus
355 often had a small loop linked to a solid globular structure. The identity of this terminal loop and
356 globular structure remains to be determined. In another selected region, several sAPEX2-tagged
357 EBOV spots were identified by manually tracing the darker stained patches on an invaginated
358 edge of electron-dense VFs. These darker-stained patches localized to the apical sides of
359 neighboring VFs where they formed a zipper-like structure (**Figure 6f**). In reconstructed
360 tomograms, the only obvious cellular structures that have direct contact with EBOV VFs are the
361 single-membrane vesicles (**Figure 6b, f**).

362 **Discussion**

363 Ebola virus (EBOV) induces formation of viral factories (VFs) in host cells that allow physical
364 separation of viral biogenesis from other cellular processes. In this study we sought to understand
365 the mechanisms by which EBOV VFs spatially accommodate and control viral RNA synthesis,
366 with a focus on the localization of the EBOV polymerase complexes within VFs.
367 The contribution of individual VF components to the internal molecular exchange within VFs
368 was poorly characterized in previous studies, even for other well-characterized viruses. Here, we
369 used a transfection-based system to supply individual EBOV components for stepwise
370 reconstitution of intracellular VF. The internal dynamics we measured using FRAP for EBOV VFs
371 produced in transfected cells are strikingly comparable to those reported for VFs in rabies virus-
372 infected cells[15]. Even though the stoichiometry of transfected viral proteins cannot fully
373 recapitulate that of virus infection, our results demonstrate the validity of using transfection-based,
374 intracellularly reconstituted VF to study phase separation behaviors of VF in living cells. Our key
375 finding is a notable reduction in the molecular exchange rate within EBOV VFs upon recruitment
376 of L to the NP-VP35 binary condensate, which is likely due to interaction of L with a fraction of
377 mobile VP35. Reducing the internal molecular exchange rate within EBOV VF could functionally
378 impact viral RNA synthesis. Longer dwell times of EBOV polymerase and its cofactors inside VFs
379 may facilitate the initiation step of EBOV polymerase-mediated viral RNA synthesis. A slower
380 internal molecular exchange rate within EBOV VFs may also facilitate concurrent NP-coating of
381 nascent RNA genome.
382 We observed that VP35 expressed in the absence of NP tends to form immobile aggregates,
383 which indirectly supports a crucial role for NP as a modulator for the internal exchange of VF
384 condensates. A previous study has shown that in the presence of VP35, a small part of the
385 intrinsically disordered region (IDR) in NP (481-500) is critical but the rest of NP C-terminal region
386 (500-739) is dispensable for VF formation. NP (481-500) also serves as a second binding site for
387 NP-VP35 interaction and interacts with the well-folded VP35 C-terminal domain[29], in addition to
388 the NP-VP35 interaction mediated by VP35 N-terminal IDR (20-48) binding to the well-folded NP
389 N-terminal region (1-457) (**Supplementary Figure 3a)**. Here we extended this finding by asking
390 whether the IDR in NP contributes to VFs internal exchange. We chose a NP mutant, NPΔ (500-
391 739), of which the majority of IDR is removed but NP-VP35 interaction is retained, so that this
392 mutant can still form condensates with VP35. Our results indicate that, in the presence of VP35,
393 the majority of IDR in NP is also dispensable for regulating VFs internal exchange. It is tempting
394 to conclude that the role of IDR in EBOV NP and VP35 in regulating VF phase behavior is coupled
395 with high-affinity heterotypic interactions with modular protein domains, as revealed in previous
396 structural studies[30,66]. This mode of interaction should be distinguished from weak interactions
397 between IDRs that have been described in many other kinds of biomolecular condensates[20].
398 Future studies can determine the role that the oligomerization domains of EBOV NP and VP35

play in condensate formation and behavior. Our work lays out the experimental foundation to further understand the role of individual protein components and their domains in modulating VF material properties and corresponding functions.

Little was previously known about the functional localization of nNSV polymerases inside cells. The lack of specific antibodies suitable for immunofluorescence labeling and the low protein abundance of viral polymerase in infected cells has made imaging of nNSV polymerases particularly challenging. An early study first identified that mCherry-tagged EBOV L polymerase homogenously locates inside VFs during infection[6]. Despite the value of mCherry for live-cell imaging, the activity of L-mCherry was only 10% that of unmodified L and the integrity of the L-mCherry was unclear due to the lack of a detection antibody against L itself at the time of the study. In contrast to insertion of a larger fluorescence protein[67], L protein can tolerate a small epitope tag without substantial loss of RNA synthesis activity[36]. A recent study using super-resolution light microscopy examined the intracellular localization of FLAG-tagged RSV L in RSV-infected cells[68]. In that study, RSV L concentrated non-uniformly at several sites inside RSV VFs. This result aligns well with our confocal microscopy findings that FLAG-tagged EBOV L formed foci inside VFs in cells reconstituted with the replication and expression of EBOV minigenome. A recombinant EBOV expressing FLAG-tagged L should be generated to further validate our findings with L localization in cells infected with authentic virus under biosafety level-4 containment.

Beyond elucidating the functional localization of EBOV polymerase L, our work links the localization pattern of EBOV L to particular types of L-mediated viral RNA synthesis. We hypothesized that VFs have distinct sub-compartments that are dedicated to viral replication or transcription. To understand EBOV L localization for replication or transcription, we separated the two processes by generating a replication-deficient EBOV minigenome (MG)[51]. We observed different EBOV L localizations in cells reconstituted with replication-competent vs. replication-deficient MG systems. When viral replication was active, the foci containing L were more widely spaced than when replication was disabled. A wider spacing of L-foci could allow more NP to permeate and become available for genome encapsidation[69]. Conversely, a narrower spacing of L-foci may reflect a switch from replication to transcription, which produces flexible viral mRNAs that are less bulky. Our result implies that rather than having distinct sub-compartments specialized for viral replication and transcription, the spatial organization of EBOV L expands and contracts according to the type or activity of ongoing viral RNA synthesis.

In addition to the spatial-functional dynamics with EBOV polymerase, we revealed an atypical, network-like morphology of EBOV VFs. In previous studies with virus-infected cells, nNSV VFs, including those induced by EBOV, appear mostly as droplet-like structures[6-8,70]. The droplet-like morphology of biomolecular condensates can be modeled by classical nucleation theory[71,72]. We did observe droplet-like VFs in EBOV-GFP-ΔVP30 infected cells, but a quarter of the cells contained network-like VFs, and sometimes both droplet-like and network-like VFs coexist in the same cell. Network-like VFs have not been reported for other viruses, except for Marburg virus[3], which is closely related to EBOV and also belongs to the *Filoviridae* family. Our research has shown that these network-like VFs are not involved in viral nucleocapsid assembly and that they lack the viral assembly factor, VP24. The absence of VP24 cannot be attributed to impaired viral gene expression since cells with network-like VFs can still express the GFP reporter encoded in the viral genome, nor to the composition of network-like VFs, because the presence of both EBOV NP and VP35 in these VFs should be sufficient to recruit VP24[33]. We believe that the presence of network-like virus factories (VFs) could indicate either 1) a stage in which the virus is transitioning from making viral mRNA and genomes to assembling the viral nucleocapsid or 2) a stage in which viral replication is not functioning properly due to dynamic arrest or asymmetry in phase separation[73,74]. To interrogate both hypotheses, one can follow the changes in the appearance of network-like VFs in live cells infected with fluorescence-tagged Ebola virus using light microscopy in a high-containment laboratory.

450 Finally, we visualized the precise 3D localization of EBOV polymerase with nanometer
451 resolution in a subcellular volume using electron-tomography. Here EBOV polymerase with the
452 split-APEX2 tag allowed localization of the polymerase among the heterogenous intracellular
453 content seen under electron microscopy[58]. Incorporating the split-APEX2 into L and VP35
454 preserved substantial levels of EBOV polymerase activity, although the valence of intermolecular
455 interaction was increased. This increased valence of intermolecular interactions in VF
456 components appeared to shift the EBOV VF morphology from the typical droplet-like to network-
457 like structures, which echoes the network-like VF we observed in EBOV-GFP-ΔVP30 infected
458 cells. Under such circumstances, we resolved multiple footprints of the EBOV polymerase
459 gathering at discrete sites in network-like EBOV VFs, where the VF phase boundary was
460 invaginated or interconnected. These sites may correlate to the EBOV L-foci under confocal light
461 microscopy.
462 Based on our confocal light and electron microscopy findings, we propose a model in which
463 EBOV polymerase molecules act in concert in a spatially restricted manner. Having a group of
464 EBOV polymerase molecules acting together on the same viral genome would compensate for
465 the low efficiency of viral RNA synthesis, as a productive viral RNA synthesis event can only
466 initiate at a single site at the 3' end of the viral genome[75]. Even so, during transcription, the EBOV
467 polymerase makes frequent stops at each intergenic region, and at each stop the polymerase
468 may detach from the genome template. How the same polymerase returns to the 3' end of the
469 viral genome and initiates a new round of RNA synthesis events is currently unclear. If a group of
470 EBOV polymerases acts on the same viral genome, some polymerases will fall off the template
471 at the gene stop signals, while other copies of the polymerase eventually reach the distal end of
472 the genome where the L gene is located. By organizing the viral genome in tandem or in another
473 coordinated way, the same group of polymerases could process more copies of the viral genome
474 and maximize viral RNA production.
475 This study has limitations. First, our results with various kinds of cell-based reconstitution
476 systems are only indicative, since these reconstitution systems cannot recapitulate the full EBOV
477 life cycle and do not supply all viral proteins. Since we are using cell-based systems, cellular
478 factors of the 293 and Vero cells used could inevitably influence VFs phase behavior and affect
479 interpretation of our results. Second, we are aware of potential artifacts with chemical fixation,
480 antibody-based immunofluorescence labeling, and split-APEX2 tagging of the viral polymerase
481 for characterization of intracellular condensates. Live-cell imaging with fluorescence protein
482 tagging may validate some of our findings. However, due to the bulkiness of fluorescence protein,
483 incorporation of a fluorescence tag does come with a price (i.e., disruption of protein function) and
484 may require high containment access for EBOV. The usage of tetracysteine tag in live cell
485 imaging[76] should be explored for EBOV proteins in the future. Nevertheless, the results of our
486 current study increase our understanding of the mechanisms associated with EBOV VFs and the
487 spatial regulation of viral RNA synthesis within. Given the similar replication strategy shared
488 among nNSVs, our findings may be applicable to other critically important nNSV pathogens, such
489 as rabies, RSV and measles virus.
490
491 **Figures and figure legends**

Figure 1

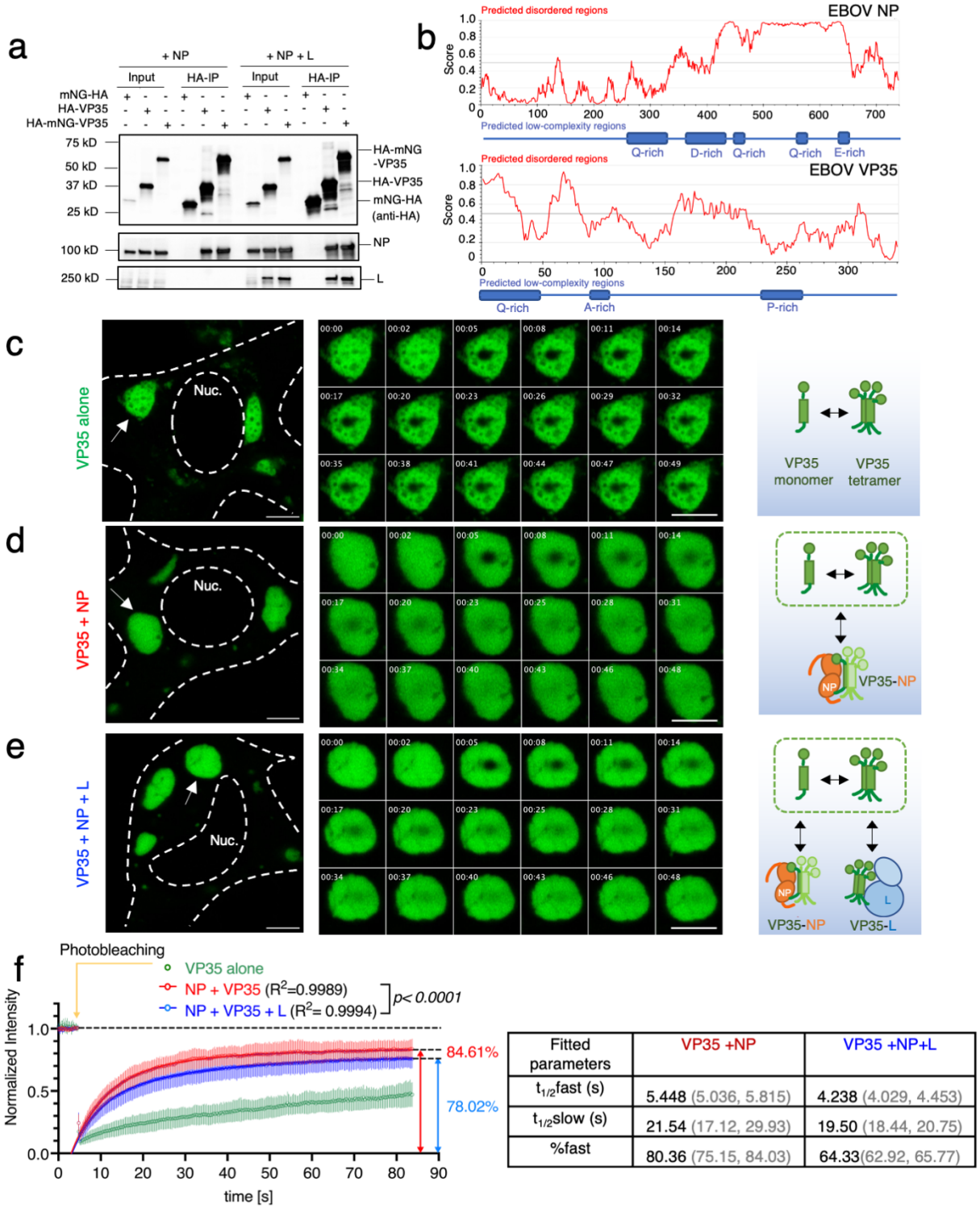

Fitted parameters	VP35 +NP	VP35 +NP+L
$t_{1/2}$fast (s)	5.448 (5.036, 5.815)	4.238 (4.029, 4.453)
$t_{1/2}$slow (s)	21.54 (17.12, 29.93)	19.50 (18.44, 20.75)
%fast	80.36 (75.15, 84.03)	64.33(62.92, 65.77)

Figure 1. Reconstituted EBOV viral factories with minimal viral protein components display viscoelastic behavior in live cells. a Bioinformatic prediction of intrinsically disordered regions and low complexity regions in the primary sequence of EBOV NP and V35 protein, using the

496 IUPred and PlaToLoCo webserver, respectively. Single letter code denotes amino acid sequence.
497 **b** Coimmunoprecipitation (co-IP) of EBOV NP and L with HA-mNG-VP35. HA-VP35 and HA-mNG
498 served as positive and negative control, respectively. Anti-HA antibody was used to detect HA-
499 mNG-VP35, HA-VP35, and HA-mNG in the input cell lysate and in HA-IP fraction. 1 mg of total
500 proteins were used in each IP reaction. Representative results from 3 biological replicates are
501 shown. Confocal microscopy of **c** VP35 **d** VP35+NP **e** VP35+NP+L condensates inside live HEK
502 293T cells 1 d post-transfection. Representative cells (N>6 cells) for each condition from 4
503 biological replicates are shown. The cell body and nucleus (Nuc.) are marked by a dashed line.
504 White arrow: individual condensate chosen for photobleaching. Image montage is composed of
505 selected frames (including t = 0 s) with an interval of 2.88 s from each time-lapse of photobleached
506 condensate displayed. The diameter of photobleached regions is 1 μm. Photobleaching occurred
507 at t = 4.8 s. Scale bars: 5 μm. Schematic of EBOV VP35-involved molecular associations
508 corresponding to each type of condensate. **f** Fluorescence recovery of mNG-HA-VP35 within the
509 photobleached region inside intracellular condensates containing VP35. Normalized intensity
510 corresponding to each time point before and after photobleaching of VP35 condensate is shown
511 in green, VP35+NP condensate is shown in red, VP35+NP+L condensate is shown in blue. Each
512 data point represents the mean with standard deviation (error bars) of N=6/9/9
513 (VP35/VP35+NP/VP35+NP+L condensates). Data points with t > 5s in red and in blue were used
514 to fit a corresponding two-phase association curve, with the normalized intensity value in
515 expressed as a percentage and the curve plateau marked on the side. Goodness of fit of each
516 curve is indicated by an R^2 value. An extra sum-of-squares F test was performed to determine
517 whether the best-fit value for unshared parameters differ between the blue and red curves. For
518 each fitted curve, the best-fit value for each kinetic parameter is shown with a 95% confidence
519 interval.
520

Figure 2

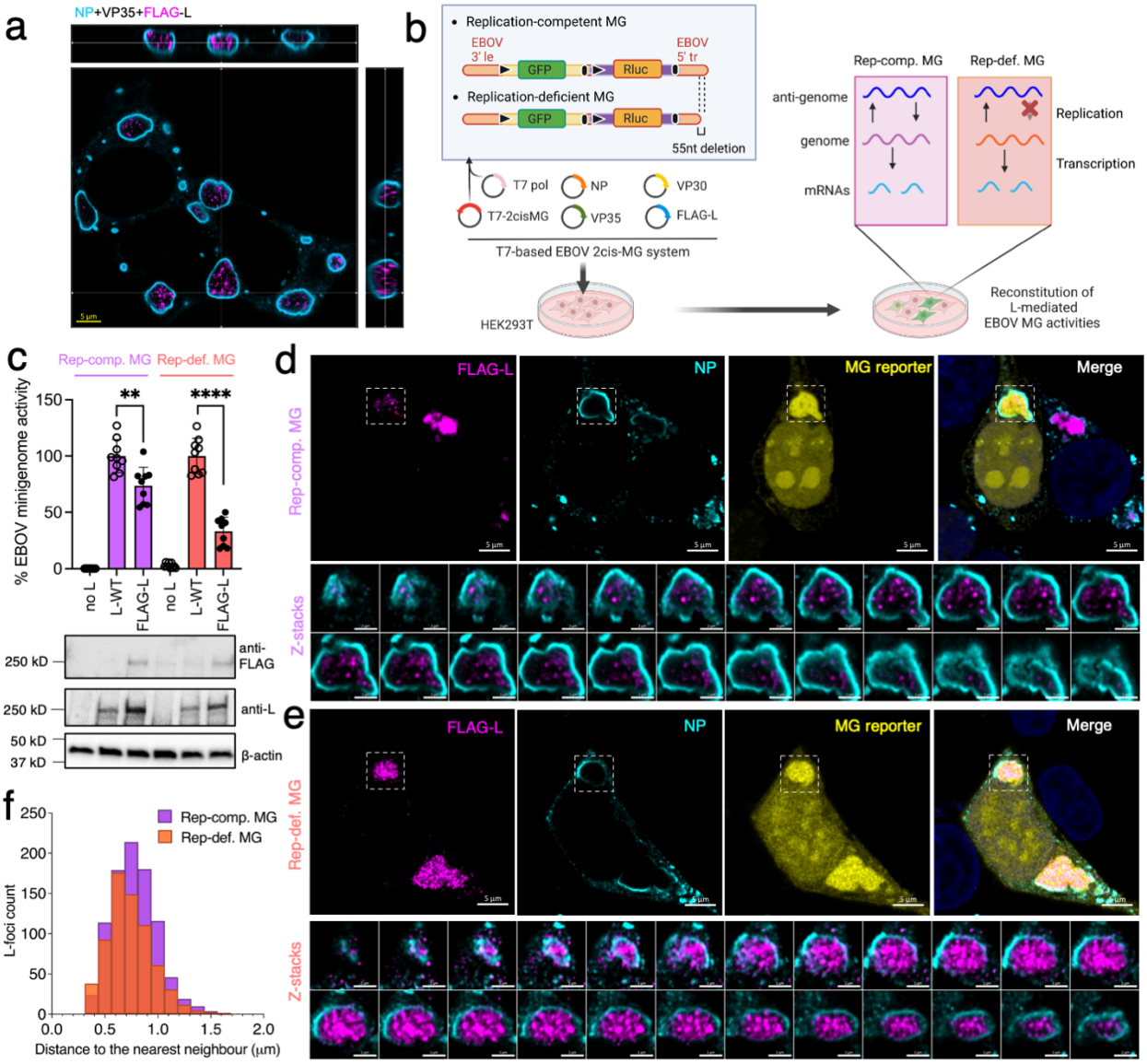

Figure 2. FLAG-tagged EBOV L cluster into foci within reconstituted viral factories. a Confocal immunofluorescence microscopy of fixed HEK 293T cells co-expressing EBOV NP, VP35 and FLAG-L at 1 d post-transfection. Represented Z-stacks in orthogonal view of 2 biological replicates each include > 4 fields of view. Scale bars: 5 μm. **b** Schematics of the T7 polymerase (T7 pol), bicistronic EBOV minigenome (2cis-MG) system with a replication competent (Rep-comp.) or replication deficient (Rep-def.) MG. 3' le: 3' leader; 5' tr: 5' trailer; black triangle: gene start; black bar: gene end. **c** Activity of FLAG-L relative to the L-WT control measured in supporting the expression of *Renilla* luciferase (Rluc) in EBOV Rep-comp. vs. Rep-def. MG. Background expression of MG assessed by excluding L in the MG system (no L). Results from 3 biological replicates with technical triplicates are shown as individual data points with mean ± SD (error bars). **, p=0.0024, ****, p<0.0001 (N=9, two-tailed, unpaired t tests with Welch's correction). Expression of FLAG-L compared to L-WT and detection of the FLAG tag analyzed by western blot using a mouse monoclonal ani-FLAG and a rabbit polyclonal anti-EBOV L antibody, respectively. Loading control: β-actin. Confocal microscopy of fixed HEK 293T cells transfected

536 with **d** Rep-comp. or **e** Rep-def. EBOV MG system at 2 d post-transfection. A representative
537 confocal image overview is shown, in which selected EBOV VFs are marked with a white box
538 (scale bars: 5 μm) and magnified in confocal z-stacks (scale bars: 2 μm). Fluorescence of the
539 GFP reporter in both Rep-comp. and Rep-def. EBOV MG is pseudo-colored in yellow for display
540 purposes. Nuclei are counterstained with Hoechst. Representative results from 4 biological
541 replicates with > 5 fields of view are shown. **f** A histogram showing the distribution of nearest
542 distances between EBOV L-foci within the same VF in the presence of Rep-comp. vs. Rep-def
543 MG, corresponding to z-stacks shown in (**d**) and (**e**). A total of 908 (Rep-comp.) or 683 (Rep-def.)
544 L-foci used in quantification.
545

546

Figure 3

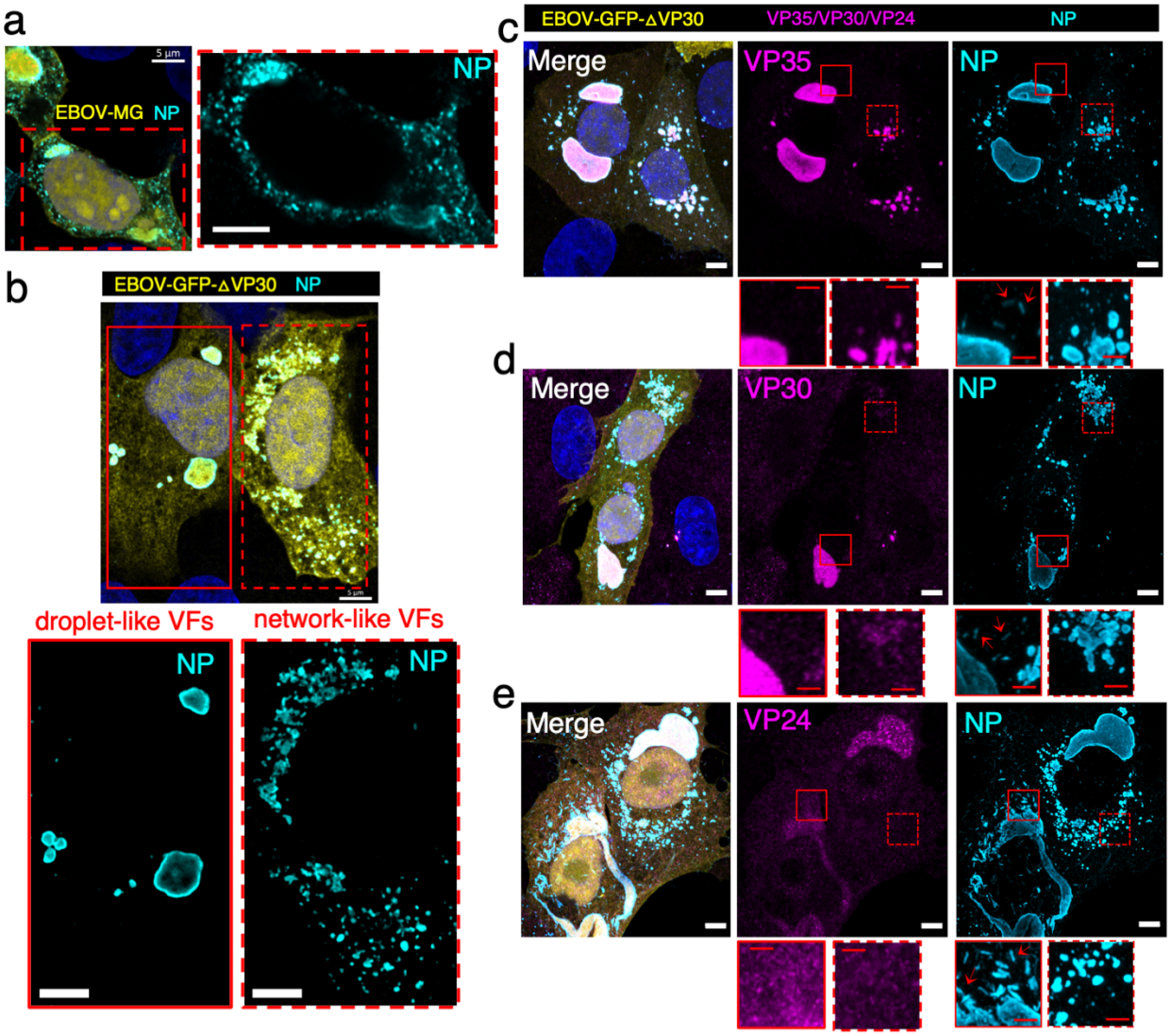

547
548 **Figure 3. Morphologically distinct EBOV viral factories in EBOV minigenome transfected**
549 **cells and EBOV-GFP-ΔVP30 infected Vero-VP30 cells. a** Confocal immunofluorescence
550 microscopy of HEK 293T cells transfected with T7-pol based, Rep-comp. EBOV MG system, at 2
551 d post transfection. L-WT was used. A representative result from 2 biological replicates with 3
552 fields of view is shown. **b** Confocal immunofluorescence microscopy of representative Vero-VP30
553 cells infected with EBOV-GFP-ΔVP30 at MOI (multiplicity of infection) = 3, 18 h post infection. A
554 total of N=39 cells from 2 biological replicates were analyzed. EBOV NP was labeled with a human
555 monoclonal anti-NP antibody paired with Alexa-568 anti-human antibody. A cell containing
556 droplet-like viral factories is magnified in single channel view with solid red outline. A cell
557 containing network-like viral factories in dashed red outline. **c, d, e** Presence of EBOV
558 nucleocapsid components in network-like viral factories was determined by double-
559 immunofluorescence analysis in virus-infected Vero-VP30 cells with similar conditions as (**b**). In
560 parallel samples, immunolabeled (**c**) EBOV VP35, (**d**) VP30, (**e**) VP24 were paired with Alexa-
561 647 secondary antibody and analyzed in conjunction with NP immunofluorescence staining.

562 Nucleus counterstained with Hoechst. Scale bars in white: 5 μm. Scale bars in red: 2 μm. Red
563 arrows: viral nucleocapsid. Orthogonal projection of confocal z-stacks shown in (**c**), (**d**), and (**e**).
564 Subcellular regions containing droplet-like viral factories are magnified in a single channel view
565 with solid red outline; regions containing network-like viral factories are shown with a dashed red
566 outline. For display purposes, fluorescence signals of the GFP reporter in Rep-comp. MG and in
567 EBOV-GFP-ΔVP30 is pseudo-colored yellow; the brightness of insects in VP30 channel (d) and
568 VP24 channel (e) are equivalently enhanced.

569

Figure 4

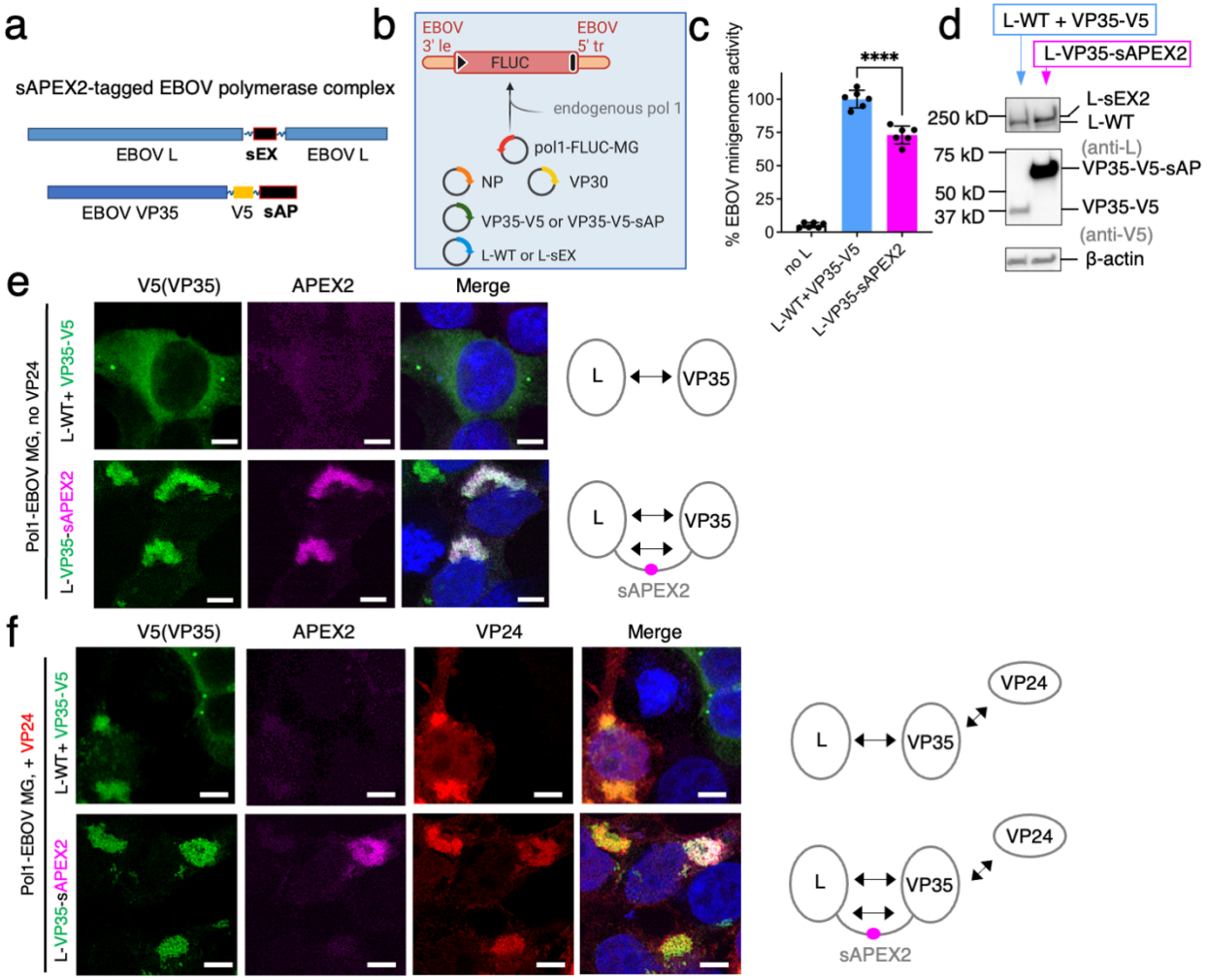

570

571 **Figure 4. Engineering and characterization of a split-APEX2 tagged EBOV polymerase**
572 **complex. a** Protein constructs of the split-APEX2 (sAPEX2)-tagged EBOV L and VP35. sAPEX
573 contains two fragments: sAP and sEX. **b** Schematic of the RNA polymerase 1(Pol1)-based,
574 monocistronic EBOV minigenome system (Pol1-EBOV MG). 3' le: 3' leader; 5' tr: 5' trailer; black
575 triangle: gene start; black bar: gene end. **c** Activity of L-sEX and VP35-V5-sEX (L-VP35-sAPEX2)
576 relative to wild-type EBOV L (L-WT) and V5-tagged VP35 (VP35-V5) control measured in
577 supporting expression of firefly luciferase (FLUC) in the EBOV MG. Background expression of
578 MG assessed by excluding L in the MG system (no L). Results from 2 biological replicates with
579 technical triplicates are shown as individual data points with mean ± SD (error bars). ****,
580 $p<0.0001$ (N=6, two-tailed, unpaired t tests with Welch's correction). **d** Expression of L-sEX
581 compared to L-WT and VP35-V5-sAP compared to VP35-V5, each analyzed by western blot
582 using a rabbit polyclonal anti-EBOV L antibody and a mouse monoclonal anti-V5 antibody,
583 respectively. Loading control: β-actin. **e** Confocal immunofluorescence microscopy of HEK 293T
584 cells transfected with the Pol1-EBOV MG system containing either L-WT +VP35-V5 or L-VP35-
585 sAPEX2, at 2 d post transfection. **f** Confocal immunofluorescence microscopy of HEK 293T cells
586 transfected with the Pol1-EBOV MG system containing either L-WT +VP35-V5 or L-VP35-

587 sAPEX2, and in the presence of VP24, at 2 d post transfection. In (**e**) and (**f**), both VP35-V5-sAP
588 and VP35-V5 were labeled with a rabbit monoclonal anti-V5 antibody paired with Alexa-488 anti-
589 rabbit antibody. Functional reconstitution of APEX2 was indicated by fluorescence signals from
590 resorufin, the product of the Amplex UltraRed, a fluorogenic peroxidase substrate for APEX2. In
591 (**f**), EBOV VP24 was labeled with a mouse monoclonal anti-VP24 antibody paired with Alexa-488
592 anti-mouse antibody. Nuclei were counterstained with Hoechst. Fluorescence signals of VP35
593 and VP24 are pseudo-colored green and red for display purposes. Scale bars: 5 μm.
594 Representative results from 2 biological replicates with >5 fields of view are shown. The valence
595 of inter-molecular interaction is depicted as double-ended arrows.
596

597
598

Figure 5

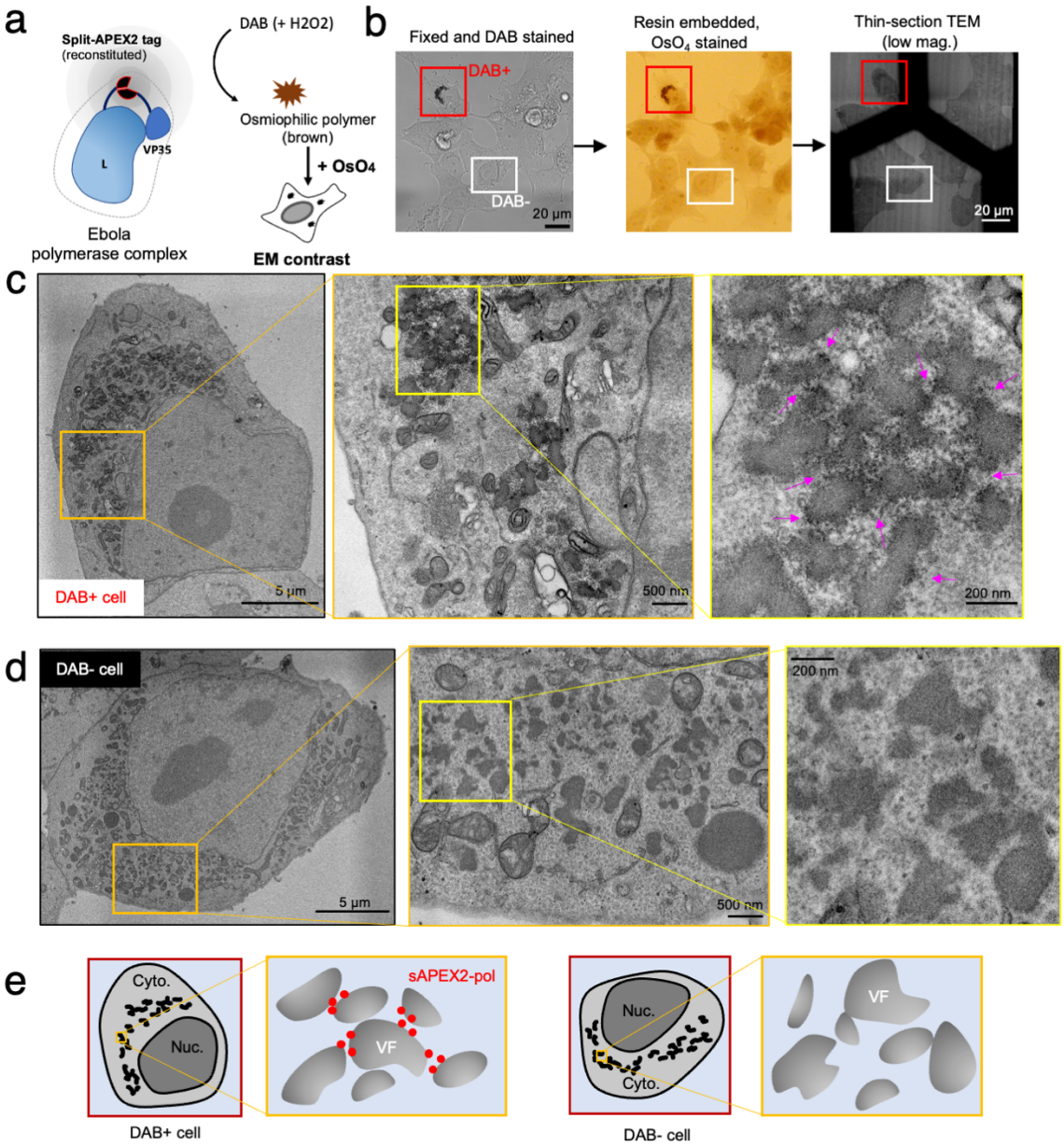

599
600 **Figure 5 Nanoscale localization of split-APEX2 tagged EBOV polymerase complex revealed**
601 **by thin-section electron microscopy (EM) a** Schematic of the functional reconstitution of
602 APEX2 upon formation of EBOV polymerase (L-VP35) complex and the resulting EM contrast
603 upon DAB-OsO_4 staining. **b** HEK 293T cells were transfected with the Pol1-EBOV-MG system
604 containing sAPEX2-tagged EBOV polymerase (L-VP35) complex and were chemically fixed with
605 2.5% glutaraldehyde and stained with DAB at 2 d post-transfection. DAB+ and DAB- cells were
606 examined by transmitted light microscopy (left) and then embedded in resin and stained with
607 OsO_4 (middle). The samples were serially sliced into 70 nm-thick sections and imaged with
608 transmission electron microscopy (TEM) at low magnification (right). Scale bars: 20 µm. **c**

609 Electron micrographs of either the overview or a cytoplasmic region of the DAB+ cell indicated in
610 (**b**) at different magnifications. Arrows: sAPEX2 mediated deposition of electron-dense Osmium.
611 **d** Electron micrographs of either the overview or a cytoplasmic region of the DAB- cell indicated
612 in (**b**) at different magnifications. Scale bars: 5 μm/500 nm/200 nm in micrographs with a
613 low/medium/high magnification. **e** Cartoons annotating the whole cell overview, the electron-
614 dense viral factories (VF) and the sAPEX2-tagged EBOV polymerases (sAPEX2-pol) in both the
615 magnified DAB+ and DAB- cell, shown in (**c**) and (**d**), respectively. Representative results from 3
616 biological replicates with multiple fields of view are shown. Cyto.: cytoplasm. Nuc.: nucleus.
617

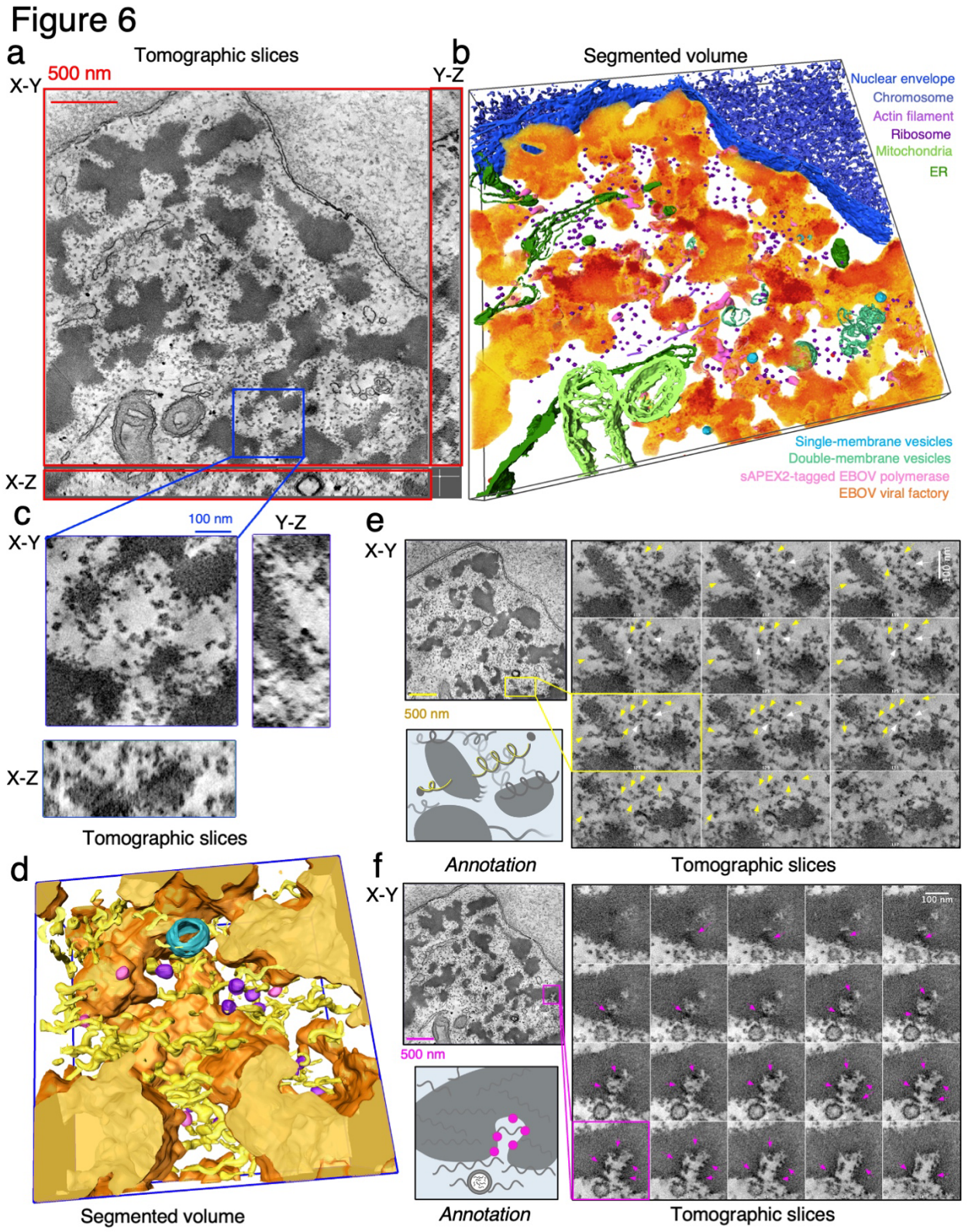

Figure 6. 3D visualization of EBOV viral factories (VFs) and sAPEX2-tagged polymerase by electron tomography. a HEK 293 cell transfected with the Pol1-EBOV-MG system containing sAPEX2-tagged EBOV polymerase (L-VP35) complex before fixation with 2.5% glutaraldehyde

622 at 2 d post-transfection. The samples were stained with DAB-OsO_4, embedded in resin and
623 sectioned into 250 nm-thick specimens. A reconstructed 3D electron tomogram of the specimen
624 originating from a DAB+ cell is shown in an orthogonal view with tomographic slices. Scale bar:
625 500 nm. **B** Segmented volume of the electron-dense EBOV VFs and surface representation of
626 numerous cellular organelles and sAPEX2-tagged EBOV polymerase, corresponding to the 3D
627 electron tomogram in (**a**). **c** Orthogonal view (with X-Y/Y-Z/X-Z plane) showing a magnified
628 volume of interest in the 3D electron tomogram in (a). Scale bar: 100 nm. **d** Segmented surface
629 representations of EBOV VFs (orange), sAPEX2-tagged EBOV polymerase (pink), viral RNP coils
630 (yellow), host ribosomes (purple), and single-membrane vesicle (blue), resulting from the
631 tomographic volume in (**c**). **e** Series of magnified tomographic slices on the X-Y plane from a
632 region containing multiple helical structures that correspond to viral RNPs. Yellow arrows pointing
633 toward one helical structure; white arrows pointing toward the branch site where multiple helical
634 structures meet. A cartoon annotation of the same region is shown on the side. **f** A series of
635 magnified tomographic slices on the X-Y plane from a region containing DAB-osmium deposits
636 that correspond to sAPEX-tagged EBOV polymerases (indicated by pink arrows) and a single-
637 membrane vesicle approaching the electron-dense VF. A cartoon annotation of the same region
638 is shown on the side. For (**e**) an (**f**), the scale bar in the tomographic overview slice and magnified
639 series represents 500 nm and 100 nm, respectively. Tomographic slice number is marked in the
640 lower left.
641

642 **Methods:**

643 **Plasmids:** If not specified, NEB HiFi assembly was used for incorporation of DNA fragments into
644 plasmid vector. To generate pCAGGS-mNG-HA-VP35, coding sequence of mNeonGreen (mNG)
645 was PCR amplified from pmNeonGreenHO-3xFLAG-G (addgene#127914), while an N-terminal
646 HA epitope tag was added to the mNG coding sequence. The resulting fragment was inserted
647 upstream of the VP35 coding sequence in pCAGGS-VP35. To generate pCAGGS-HA-VP35
648 control plasmid, a DNA fragment containing a HA epitope tag followed by a flexible linker was
649 synthesized and added to the N-terminus of VP35 coding frame. To generate pCMV-mNG-HA
650 control plasmid, a HA epitope tag was added to the C-terminus of mNG coding sequence. To
651 generate pCAGGS-VP35-V5-sAP, the fragment of sAP was PCR amplified from
652 FKBP_V5_AP_NEX_pLX304 (addgene#120912) and cloned into the intermediate vector
653 pcDNA5-VP35. The fragment of VP35-V5-sAP was subcloned to pCAGGS plasmid using
654 restriction sites Xho1 and Nhe1 and standard ligation method. To generate pCAGGS-VP35-V5
655 control plasmid, the fragment of VP35-V5 was PCR amplified with an addition of a stop codon
656 and Bgl2 restriction site, and was then incorporated into pCAGGS backbone using Kpn1 and Bgl2
657 restriction sites.
658 To generate pCAGGS-FLAG-L, a DNA fragment containing a 2xFLAG epitope tag followed
659 by a flexible linker was synthesized and added to the N-terminus of L coding frame. To generate
660 pCEZ-L-sEX, a fragment of L coding sequence was first subcloned into a pFastbacDual
661 intermediate plasmid using the natural restriction sites Pac1 and Hpa1. From there, coding
662 sequence of sEX was PCR amplified from HA-Halotag-FRB-EX-NES-pLX304 (addgene
663 #120913), flanked by two flexible linkers and was internally inserted to L fragment at the position
664 1705/1706 (TTIP/Q). The L-sEX fragment was shuffled back to the pCEZ-L backbone using the
665 same restriction sites Pac1 and Hpa1.
666 To generate pT7-2cis-MG-Replication competent (Rep-Comp.), the coding sequence of VP40,
667 GP and VP24, including non-coding sequences VP40/GP and VP30/VP24 in between were
668 removed from pT7-4cis-EBOV-vRNA-eGFP plasmid[34], while the coding sequence of *Renilla*
669 luciferase was inserted downstream of the non-coding sequence NP/VP35 and reassembled. To
670 generate pT7-2cis-MG-Replication deficient (Rep-def.), the last 55 nucleotide of the 5' trailer
671 sequence in pT7-2cis-MG-Rep-comp. plasmid was removed by PCR and re-assembled. Other
672 supporting plasmids used in T7-based EBOV minigenome system were obtained from Dr.
673 Thomas Hoenen (Friedrich-Loeffler-Institute). Plasmids used in Pol1-based EBOV minigenome
674 system were obtained from Dr. Yoshihiro Kawaoka (University of Wisconsin Madison).

675 **Cell lines and virus:** Human embryonic kidney cells HEK 293T (ATCC reference: CRL-3216)
676 were originally purchased from the ATCC organization. Vero cells stabling expressing Ebola virus
677 VP30 protein (Vero-VP30) were obtained from Dr. Yoshihiro Kawaoka (University of Wisconsin
678 Madison). Both cell lines were maintained in Dulbecco's modified Eagle medium (DMEM-
679 GlutaMAX) supplemented with 4.5 g/L D-Glucose, 10% fetal bovine serum (FBS), penicillin
680 (100 U/mL), streptomycin (100 µg/mL). In addition, puromycin (5 µg/mL) was included in the
681 culture media while maintaining Vero-VP30 cells but excluded for infection experiment. The
682 biologically contained Ebola virus, EBOV-ΔVP30-GFP was generated in HEK 293T cells and
683 grown in Vero-VP30 cells as previously described[52].

684 **Fluorescence Recovery After Photobleaching (FRAP):** IBIDI µ-slides (8 wells high-precision
685 glass bottom) were treated with human fibronectin (50 mg/mL) for 20 minutes at 37°C incubator,
686 prior to HEK 293T cells seeding ($4X10^4$ cells/well). Twenty-four hours later, the monolayer was
687 transfected with plasmids in three different combinations: 1) 125 ng of pCAGGS-mNG-HA-VP35
688 and 1 µg of pCAGGS-vector control; 2) 125 ng of pCAGGS-mNG-HA-VP35, 125 ng of pCAGGS-
689 NP, and 875 ng of pCAGGS-vector control; 3) 125 ng of pCAGGS-mNG-HA-VP35, 125 ng of

690 pCAGGS-NP, and 875 ng of pCAGGS-L (wild-type). Transfected cells were incubated with
691 complete FluoroBrite DMEM (+1x Glutamax, 10% FBS) for imaging. Time series were acquired
692 using ZEISS laser scanning microscope (LSM880) with an Airyscan detector while live cells
693 sample were kept in caged incubator maintaining 37˚C and 5% CO_2. mNG fluorescence was
694 excited with a 488 nm argon laser and detected with a 63x 1.4NA oil immersion objective (Plan-
695 Apochromat), with a combination of bandpass filters (420-480) and (495-550). Using a frame rate
696 of 240 millisecond per frame and 0.4% of 488 nm laser, 20 frames were recorded pre-bleach, and
697 then 330 frames were recorded post-bleach under the Airyscan fast mode. This duration of post-
698 bleach image acquisition was experimentally determined by the time when fluorescence recovery
699 reached a plateau. For photobleaching, 488 nm laser at 80% was used to pulse-bleach a spot
700 size of 1 micron in diameter in the center of large condensates, until the fluorescence intensity of
701 the bleach spot reduced to 30% of the prebleached value.
702
703 **FRAP quantification and interpretation:** Time series in which the bleached object moved during
704 post-bleach phase were manually identified and removed from data analysis because the
705 fluorescence intensity of the bleached spot could not be accurately measured in ImageJ/FIJI[77].
706 For each bleach event, double normalization of the FRAP curve was performed using ImageJ/FIJI
707 as described[15]. To correct unintentional photobleaching due to time-series acquisition, in every
708 frame, fluorescence intensity of the bleached spot (1 μm in diameter) was first normalized to the
709 mean intensity of an unbleached spot (1 μm in diameter) of another condensate in the same field
710 of view. The resulting values after correction for all frames were further normalized to the average
711 intensity of the last 10 pre-bleach frames. The background intensity in each field of view was
712 negligible as it was lower than 0.5% of the average intensity of viral factory condensates.
713 Due to biological mobility of the intracellular condensate and the cellular specimens during
714 imaging, we could not accurately measure the bleach pulses-induced fluorescence loss in the
715 whole condensate. Instead, we assessed this parameter in the averaged fluorescence decay of
716 internal reference-regions inside the same condensate that was photobleached but are away from
717 the bleached spot. Double normalized data from 6-9 cells in a total of three independent
718 experiments were pooled. Means with standard deviation of double normalized intensity were
719 plotted as a function of time, of which post-bleach data-points were fitted to a two-phase
720 association model in GraphPad prism, according to previously described methods[78]. Best-fit
721 values with 95% confidence interval and goodness of fit indicated by R^2 for each data set were
722 reported.

723 $$A_{fast} = (Plateau - Y_0) \times \%Fast$$
724 $$A_{slow} = (Plateau - Y_0) \times (1 - \%Fast)$$
725 $$Y(t) = Y_0 + A_{fast}\left(1 - e^{-k_{fast}t}\right) + A_{slow}(1 - e^{-k_{slow}t})$$

726 Fluorescence recovery of a sub-area within the VF condensate describes a combined rate of
727 molecular exchange that occur within the VF condensate and occur between the VF and the
728 cytoplasm. However, because the fluorescence intensity of molecules in the VF condensate is
729 ~200-folds higher than that of the diffused molecules in the cytoplasm and the total VF condensate
730 is significantly larger than the photo-bleached spot. The combined rate measured in the current
731 work could approximate the internal exchange rate within the VF condensate.

732 **Immunofluorescence staining and confocal light microscopy:** Fixation and staining was
733 performed as described[79].
734 For samples shown in supplementary Figure S1b, human monoclonal anti-Ebola virus NP
735 (1:2000), mouse monoclonal anti-Ebola virus VP35 (1:500), and rabbit polyclonal anti-Ebola virus
736 L antibody (1:200) were used as the primary antibodies, goat anti-human Alexa-568 (1:1000),

737 goat anti-mouse Alexa-647 (1:500), and goat anti-rabbit Alexa-568 (1:500) were used as the
738 secondary antibodies.
739 For samples shown in Figure 2, human monoclonal anti-Ebola virus NP (1:2000) and mouse
740 monoclonal anti-FLAG (1:100) antibody were used as the primary antibodies, goat anti-human
741 Alexa-568 (1:1000) and goat anti-mouse Alexa-647 (1:500) were used as the secondary
742 antibodies.
743 For samples shown in Figure 3, human monoclonal anti-NP (1:2000) and goat anti-human
744 Alexa-568 (1:1000) were used.
745 For samples shown in Figure 4, rabbit monoclonal anti-V5 (1:500) and mouse monoclonal
746 anti-Ebola VP24 (1:1000, a kind gift from Dr. Yoshihiro Kawaoka) were used as the primary
747 antibodies, goat anti-human Alexa-568 (1:1000) and goat anti-mouse Alexa-647 (1:500) were
748 used as the secondary antibodies. In addition, trans-complemented APEX2 was stained with
749 Amplex UltraRed at 100 nM (with 0.02% H_2O_2 in DPBS) on ice for 20 minutes prior to fixation.
750 Unreacted Amplex UltraRed was washed off with DPBS.
751 Single-plane confocal images or confocal Z-stacks (interval= 0.224 μm) were acquired with
752 the ZEISS laser scanning microscope (LSM880)-Airyscan system under the superresolution
753 mode, using a plan-apochromat 20x/0.8 numerical aperture M27 objective or an alpha plan-
754 apochromat 63×/1.46 numerical aperture oil Korr M27 objective. All images or stacks that are
755 shown or quantified were Airyscan processed using the Zen black (ZEISS) build-in function.
756 For supplementary Figure 1C, quantification and counting of reconstituted Ebola viral factories
757 (VFs) in single-plane confocal images using ImageJ/Fiji. HEK 293T cells were prepared using
758 identical transfection conditions described in FRAP experiment. VFs were identified on the basis
759 of mNG-fluorescence and analyzed for the count and size distribution using the analyze particle
760 function.
761 For Figure 2f, 3D segmentation of Ebola viral factories in confocal Z-stacks was performed in
762 Imaris 9.9.1 using the surface function and automatically thresholding the GFP intensity;
763 segmentation of FLAG-tagged Ebola virus L-foci inside each viral factory was performed using
764 the spot function and automatically thresholding the fluorescence intensity of FLAG-L with an
765 estimated diameter for each spot as 0.5 μm, which generates specific values of distance to
766 nearest neighbor for every random pair of segmented spot.

767 **Virus infection with EBOV-GFP-ΔVP30**: Vero-VP30 cells ($4X10^4$ cells/well) were seeded in
768 IBIDI μ-slides (8 wells high-precision glass bottom). Twenty-four hours later, the monolayer was
769 incubated with EBOV-ΔVP30-GFP (MOI=3 foci-forming unit/cell) on ice. After 1 hour, the
770 monolayer was washed three times with cold DPBS to remove unbound virions and was moved
771 to the 37˚C incubator. Infection was terminated after 16 hours. Infected cells were inactivated with
772 4% PFA for 15 minutes.

773 **Thin-section TEM with DAB staining**: Sample preparation was adapted from[80]. Mattek 35 mm
774 dish with NO#1.5 gridded glass bottom (P35G-1.5-14-C-GRD) was treated with human fibronectin
775 (50 mg/mL) for 1 hour at 37°C incubator, prior to HEK 293T cells seeding ($1X10^5$ cells/well).
776 Twenty-four hours later, the monolayer was either untreated or transfected with plasmids in two
777 different combinations: 1) EBOV Pol1-MG system containing VP35-V5 and L-WT; 2) EBOV Pol1-
778 MG system containing sAPEX2 tagged L-VP35.
779 For the first combination, 250 ng of pCEZ-NP, 187.5 ng of pCEZ-VP30, 250 ng of pCEZ-
780 VP35-V5, 156.25 ng of pHH21-3E5E-fluc, and 1875 ng of pCEZ-L were used in the co-
781 transfection mix for each 35 mm dish. For the second combination, 250 ng of pCEZ-NP, 187.5 ng
782 of pCEZ-VP30, 250 ng of pCEZ-VP35-V5-sAP, 156.25 ng of pHH21-3E5E-fluc, and 1875 ng of
783 pCEZ-L-sEX were used in the co-transfection mix for each 35 mm dish.
784 Forty-eight hours post-transfection, cells were fixed first in 2.5% glutaraldehyde-0.1 M
785 cacodylate buffer pH 7.4 + 2 mM $CaCl_2$ at room temperature for 1 minute, then fixed in pre-chilled

786 2.5% glutaraldehyde-0.1 M cacodylate buffer pH 7.4 + 2 mM $CaCl_2$ on ice for 1 hour, and were
787 washed three times with cold 0.1 M cacodylate buffer pH 7.4 (cacodylate buffer). Unreacted
788 fixative in samples was quenched with cold 20 mM Glycine solution for 5 min on ice, followed by
789 three washes with cold cacodylate buffer. Samples were stained with 2.5 mM DAB (Sigma
790 #D8001)-0.1 M cacodylate solution in the presence of 1/1000V of 30% H_2O_2 for 45 minutes on
791 ice and washed three times with cold cacodylate buffer.
792 Brown DAB stain in samples was confirmed under light microscopy. Samples were then
793 stained in 1% osmium+1.5% potassium Ferrocyanide in 0.1 M cacodylate buffer on ice for 1 hour
794 and washed three times with cacodylate buffer. Samples were dehydrated with increasing
795 concentrations of ethanol (20%, 50%, 70%, 90%, 100%, 100%, 3 minutes each) and washed
796 once in room temperature anhydrous ethanol. Samples were then infiltrated with Durcupan ACM
797 resin (Electron Microscopy Sciences) using a mixture of anhydrous ethanol: resin (1V:1V) for 30
798 minutes, then with 100% resin overnight, followed by 48 hours polymerization step at 60 °C.
799 Ultrathin sections with a 70 mm thickness of embedded specimen were mounted on 200 mesh
800 hexagonal copper grids with no post-staining step. Electron micrographs were collected using a
801 FEI Tecnai Spirit transmission electron microscope operating at 120 kV.

802 **Electron tomography and data processing:** Electron tomography was performed using a
803 300kV Titan Halo equipped with an 8k x 8k direct detector (DE64, Direct Electron). During the
804 procedure, semi-thick (~250 nm) sections of the resin-embedded specimen were imaged at
805 different orientations using a 4-tilt acquisition scheme as described[81], for which the specimen was
806 tilted from -60 to +60 degrees every 0.25 degree at four different azimuthal orientation. For
807 aligning the micrographs, 5 nm colloidal gold particles were deposited on each side of the sections
808 to serve as fiducial markers. The TEM magnification was set at 11,000x, corresponding to a raw
809 pixel size of 0.36 nm. Tomograms were generated with an iterative reconstruction procedure[81],
810 and was binned by a factor of 4 for display and for volume segmentation using Amira 2020 3.1.
811 software. Membrane organelles were segmented manually combined with automatic thresholding.
812 Ribosomes were segmented manually. EBOV viral factories and sAPEX2-tagged EBOV
813 polymerase were segmented with a combination of automatic thresholding and the TopHat tool.

814 **EBOV minigenome assays**: Transfection and activity quantification with Pol1-based
815 monocistronic EBOV minigenome system was adapted from[35] and described previously[79].
816 Transfection with the T7 pol-based EBOV bicistronic minigenome system was adapted from[34].
817 Activity of bicistronic minigenome system was measured in *Renilla* luciferase assay. For each
818 transfection condition, the same cell lysates used in luciferase assay, were pooled from triplicated
819 assay wells and analyzed in western blot.

820 **Coimmunoprecipitation (coIP):** Co-IP reactions were performed as previously described[79]. HEK
821 293T cells ($1X10^6$ cells/well) were seeded in 6-wells plates. Twenty-four hours later, cells in each
822 well were transfected with 500 ng of pCMV-mNG-HA or pCAGGS-HA-VP35 or pCAGGS-mNG-
823 HA-VP35 plasmid combined with 500 ng of pCAGGS-NP, with and without 1 µg of pCAGGS-L,
824 using TransIT-LT1 transfection reagent. HA-affinity matrix was used to pull-down protein
825 complexes containing HA-tagged proteins. Equal amount of total protein (1 mg) was used in each
826 co-IP reaction.

827 **Statistical analysis:** Data shown in Figure 2c, 4a and supplementary Figure 1a were calculated
828 and plotted in mean with SD. Statistical analysis were analyzed by two-tailed unpaired t-test with
829 Welch's correction. P values were indicated in figure legends. Data shown in Figure 1f were
830 analyzed using an extra sum-of-squares F test to compare whether the best-fit values of *%Fast*,
831 k_{fast} and k_{slow} differ between two datasets. The resulting *p* value indicating the statistical
832 significance of the difference was reported in the figure.

Acknowledgments: We thank Dr. Yoshihiro Kawaoka (University of Wisconsin) for providing the Pol1-based Ebola minigenome system, sharing the anti-VP30 and anti-VP24 antibodies and the EBOV-GFP-ΔVP30 system. We thank Dr. Reika Watanabe (LJI) for providing the EBOV-GFP-ΔVP30 virus stock. We thank Dr. Thomas Hoenen (Friedrich-Loeffler-Institute) for sharing the Ebola tetracistronic trVLP system. We thank Diptiben Parekh (LJI) for plasmid preparations, Dr. Sharon Schendel (LJI) for manuscript editing, NIH S10OD021831 for sponsoring the Zeiss LSM 880 microscope at the LJI microscopy core facility and an Imaging Scientist grant (2019-198153) from the Chan Zuckerberg Initiative to S.M. (LJI). We thank NIH R24GM137200 and S10OD021784 to M.H.E. (UCSD) in support of the National Center for Microscopy and Imaging Research. This research was supported by institutional funds of La Jolla Institute for Immunology to E.O.S. (LJI). J.F. was supported by the Donald E. and Delia B. Baxter Foundation Fellowship.

Author contributions: J.F. conceived the study and wrote the paper under the supervision of E.O.S.; J.F., G.C. and S.M. designed the experiments, J.F., G.C., S.P., S.M., C.H., and A.A. performed the experiments; J.F., G.C., analyzed the data, M.H.E. supervised the data acquisition and interpretation for electron microscopy analysis, A.A.D. contributed to data interpretation of intracellular condensates. All authors edited and approved the paper.

Data availability: All data supporting the findings of this study are available within the paper and its supplementary information. Source data are provided with this paper.

851 **References**
852

853 1 Alenquer, M. *et al.* Influenza A virus ribonucleoproteins form liquid organelles at
854 endoplasmic reticulum exit sites. *Nat Commun* **10**, 1629, doi:10.1038/s41467-019-09549-
855 4 (2019).
856 2 Cifuentes-Munoz, N., Branttie, J., Slaughter, K. B. & Dutch, R. E. Human Metapneumovirus
857 Induces Formation of Inclusion Bodies for Efficient Genome Replication and Transcription.
858 *J Virol* **91**, doi:10.1128/JVI.01282-17 (2017).
859 3 Dolnik, O., Stevermann, L., Kolesnikova, L. & Becker, S. Marburg virus inclusions: A virus-
860 induced microcompartment and interface to multivesicular bodies and the late
861 endosomal compartment. *Eur J Cell Biol* **94**, 323-331, doi:10.1016/j.ejcb.2015.05.006
862 (2015).
863 4 Geiger, F. *et al.* Liquid-liquid phase separation underpins the formation of replication
864 factories in rotaviruses. *EMBO J* **40**, e107711, doi:10.15252/embj.2021107711 (2021).
865 5 Heinrich, B. S., Cureton, D. K., Rahmeh, A. A. & Whelan, S. P. Protein expression redirects
866 vesicular stomatitis virus RNA synthesis to cytoplasmic inclusions. *PLoS Pathog* **6**,
867 e1000958, doi:10.1371/journal.ppat.1000958 (2010).
868 6 Hoenen, T. *et al.* Inclusion bodies are a site of ebolavirus replication. *J Virol* **86**, 11779-
869 11788, doi:10.1128/JVI.01525-12 (2012).
870 7 Jobe, F., Simpson, J., Hawes, P., Guzman, E. & Bailey, D. Respiratory Syncytial Virus
871 Sequesters NF-kappaB Subunit p65 to Cytoplasmic Inclusion Bodies To Inhibit Innate
872 Immune Signaling. *J Virol* **94**, doi:10.1128/JVI.01380-20 (2020).
873 8 Lahaye, X. *et al.* Functional characterization of Negri bodies (NBs) in rabies virus-infected
874 cells: Evidence that NBs are sites of viral transcription and replication. *J Virol* **83**, 7948-
875 7958, doi:10.1128/JVI.00554-09 (2009).
876 9 Lee, C. H. *et al.* Reovirus Nonstructural Protein sigmaNS Recruits Viral RNA to Replication
877 Organelles. *mBio* **12**, e0140821, doi:10.1128/mBio.01408-21 (2021).
878 10 Ringel, M. *et al.* Nipah virus induces two inclusion body populations: Identification of
879 novel inclusions at the plasma membrane. *PLoS Pathog* **15**, e1007733,
880 doi:10.1371/journal.ppat.1007733 (2019).
881 11 Zhou, Y., Su, J. M., Samuel, C. E. & Ma, D. Measles Virus Forms Inclusion Bodies with
882 Properties of Liquid Organelles. *J Virol* **93**, doi:10.1128/JVI.00948-19 (2019).
883 12 Feric, M. *et al.* Coexisting Liquid Phases Underlie Nucleolar Subcompartments. *Cell* **165**,
884 1686-1697, doi:10.1016/j.cell.2016.04.047 (2016).
885 13 Whelan, S. P., Barr, J. N. & Wertz, G. W. Transcription and replication of nonsegmented
886 negative-strand RNA viruses. *Curr Top Microbiol Immunol* **283**, 61-119, doi:10.1007/978-
887 3-662-06099-5_3 (2004).
888 14 Heinrich, B. S., Maliga, Z., Stein, D. A., Hyman, A. A. & Whelan, S. P. J. Phase Transitions
889 Drive the Formation of Vesicular Stomatitis Virus Replication Compartments. *mBio* **9**,
890 doi:10.1128/mBio.02290-17 (2018).
891 15 Nikolic, J. *et al.* Negri bodies are viral factories with properties of liquid organelles. *Nat*
892 *Commun* **8**, 58, doi:10.1038/s41467-017-00102-9 (2017).

893 16 Guseva, S. *et al.* Measles virus nucleo- and phosphoproteins form liquid-like phase-
894 separated compartments that promote nucleocapsid assembly. *Sci Adv* **6**, eaaz7095,
895 doi:10.1126/sciadv.aaz7095 (2020).
896 17 Boggs, K. B. *et al.* Human Metapneumovirus Phosphoprotein Independently Drives Phase
897 Separation and Recruits Nucleoprotein to Liquid-Like Bodies. *mBio* **13**, e0109922,
898 doi:10.1128/mbio.01099-22 (2022).
899 18 Risso-Ballester, J. *et al.* A condensate-hardening drug blocks RSV replication in vivo.
900 *Nature* **595**, 596-599, doi:10.1038/s41586-021-03703-z (2021).
901 19 Alberti, S., Gladfelter, A. & Mittag, T. Considerations and Challenges in Studying Liquid-
902 Liquid Phase Separation and Biomolecular Condensates. *Cell* **176**, 419-434,
903 doi:10.1016/j.cell.2018.12.035 (2019).
904 20 Banani, S. F., Lee, H. O., Hyman, A. A. & Rosen, M. K. Biomolecular condensates: organizers
905 of cellular biochemistry. *Nat Rev Mol Cell Biol* **18**, 285-298, doi:10.1038/nrm.2017.7
906 (2017).
907 21 Brangwynne, Clifford P., Tompa, P. & Pappu, Rohit V. Polymer physics of intracellular
908 phase transitions. *Nature Physics* **11**, 899-904, doi:10.1038/nphys3532 (2015).
909 22 Ruff, K. M. *et al.* Sequence grammar underlying the unfolding and phase separation of
910 globular proteins. *Mol Cell* **82**, 3193-3208 e3198, doi:10.1016/j.molcel.2022.06.024
911 (2022).
912 23 Boeynaems, S. *et al.* Spontaneous driving forces give rise to protein-RNA condensates
913 with coexisting phases and complex material properties. *Proc Natl Acad Sci U S A* **116**,
914 7889-7898, doi:10.1073/pnas.1821038116 (2019).
915 24 Harmon, T. S., Holehouse, A. S., Rosen, M. K. & Pappu, R. V. Intrinsically disordered linkers
916 determine the interplay between phase separation and gelation in multivalent proteins.
917 *Elife* **6**, doi:10.7554/eLife.30294 (2017).
918 25 *Ebola virus disease*, <https://www.who.int/news-room/fact-sheets/detail/ebola-virus-
919 disease> (2022).
920 26 *History of Ebola Virus Disease (EVD) Outbreaks*,
921 <https://www.cdc.gov/vhf/ebola/history/chronology.html> (2022).
922 27 Wyers, M. *et al.* Histopathological and immunohistochemical studies of lesions associated
923 with Ebola virus in a naturally infected chimpanzee. *J Infect Dis* **179 Suppl 1**, S54-59,
924 doi:10.1086/514300 (1999).
925 28 Becker, S., Rinne, C., Hofsass, U., Klenk, H. D. & Muhlberger, E. Interactions of Marburg
926 virus nucleocapsid proteins. *Virology* **249**, 406-417, doi:10.1006/viro.1998.9328 (1998).
927 29 Miyake, T. *et al.* Ebola Virus Inclusion Body Formation and RNA Synthesis Are Controlled
928 by a Novel Domain of Nucleoprotein Interacting with VP35. *J Virol* **94**,
929 doi:10.1128/JVI.02100-19 (2020).
930 30 Kirchdoerfer, R. N., Abelson, D. M., Li, S., Wood, M. R. & Saphire, E. O. Assembly of the
931 Ebola Virus Nucleoprotein from a Chaperoned VP35 Complex. *Cell Rep* **12**, 140-149,
932 doi:10.1016/j.celrep.2015.06.003 (2015).
933 31 Trunschke, M. *et al.* The L-VP35 and L-L interaction domains reside in the amino terminus
934 of the Ebola virus L protein and are potential targets for antivirals. *Virology* **441**, 135-145,
935 doi:10.1016/j.virol.2013.03.013 (2013).

936 32 Kirchdoerfer, R. N., Moyer, C. L., Abelson, D. M. & Saphire, E. O. The Ebola Virus VP30-NP
937 Interaction Is a Regulator of Viral RNA Synthesis. *PLoS Pathog* **12**, e1005937,
938 doi:10.1371/journal.ppat.1005937 (2016).
939 33 Banadyga, L. *et al.* Ebola virus VP24 interacts with NP to facilitate nucleocapsid assembly
940 and genome packaging. *Sci Rep* **7**, 7698, doi:10.1038/s41598-017-08167-8 (2017).
941 34 Schmidt, M. L., Tews, B. A., Groseth, A. & Hoenen, T. Generation and Optimization of a
942 Green Fluorescent Protein-Expressing Transcription and Replication-Competent Virus-
943 Like Particle System for Ebola Virus. *J Infect Dis* **218**, S360-S364, doi:10.1093/infdis/jiy405
944 (2018).
945 35 Jasenosky, L. D., Neumann, G. & Kawaoka, Y. Minigenome-based reporter system suitable
946 for high-throughput screening of compounds able to inhibit Ebolavirus replication and/or
947 transcription. *Antimicrob Agents Chemother* **54**, 3007-3010, doi:10.1128/AAC.00138-10
948 (2010).
949 36 Bodmer, B. S. & Hoenen, T. Assessment of Life Cycle Modeling Systems as Prediction Tools
950 for a Possible Attenuation of Recombinant Ebola Viruses. *Viruses* **14**,
951 doi:10.3390/v14051044 (2022).
952 37 Noda, T., Hagiwara, K., Sagara, H. & Kawaoka, Y. Characterization of the Ebola virus
953 nucleoprotein-RNA complex. *J Gen Virol* **91**, 1478-1483, doi:10.1099/vir.0.019794-0
954 (2010).
955 38 Shu, T. *et al.* Ebola virus VP35 has novel NTPase and helicase-like activities. *Nucleic Acids*
956 *Res* **47**, 5837-5851, doi:10.1093/nar/gkz340 (2019).
957 39 Watanabe, S., Noda, T. & Kawaoka, Y. Functional mapping of the nucleoprotein of Ebola
958 virus. *J Virol* **80**, 3743-3751, doi:10.1128/JVI.80.8.3743-3751.2006 (2006).
959 40 Bruhn, J. F. *et al.* Crystal Structure of the Marburg Virus VP35 Oligomerization Domain. *J*
960 *Virol* **91**, doi:10.1128/JVI.01085-16 (2017).
961 41 Chanthamontri, C. K. *et al.* The Ebola Viral Protein 35 N-Terminus Is a Parallel Tetramer.
962 *Biochemistry* **58**, 657-664, doi:10.1021/acs.biochem.8b01154 (2019).
963 42 Zinzula, L. *et al.* Structures of Ebola and Reston Virus VP35 Oligomerization Domains and
964 Comparative Biophysical Characterization in All Ebolavirus Species. *Structure* **27**, 39-54
965 e36, doi:10.1016/j.str.2018.09.009 (2019).
966 43 Noda, T., Kolesnikova, L., Becker, S. & Kawaoka, Y. The importance of the NP: VP35 ratio
967 in Ebola virus nucleocapsid formation. *J Infect Dis* **204 Suppl 3**, S878-883,
968 doi:10.1093/infdis/jir310 (2011).
969 44 Leung, D. W. *et al.* Structural basis for dsRNA recognition and interferon antagonism by
970 Ebola VP35. *Nat Struct Mol Biol* **17**, 165-172, doi:10.1038/nsmb.1765 (2010).
971 45 Chen, Y. G. & Hur, S. Cellular origins of dsRNA, their recognition and consequences. *Nat*
972 *Rev Mol Cell Biol* **23**, 286-301, doi:10.1038/s41580-021-00430-1 (2022).
973 46 Sprague, B. L. & McNally, J. G. FRAP analysis of binding: proper and fitting. *Trends Cell Biol*
974 **15**, 84-91, doi:10.1016/j.tcb.2004.12.001 (2005).
975 47 Nelson, E. V. *et al.* Ebola Virus Does Not Induce Stress Granule Formation during Infection
976 and Sequesters Stress Granule Proteins within Viral Inclusions. *J Virol* **90**, 7268-7284,
977 doi:10.1128/JVI.00459-16 (2016).

978 48 Zhu, L. *et al.* Ebola virus VP35 hijacks the PKA-CREB1 pathway for replication and
979 pathogenesis by AKIP1 association. *Nat Commun* **13**, 2256, doi:10.1038/s41467-022-
980 29948-4 (2022).
981 49 Farag, M. *et al.* Condensates formed by prion-like low-complexity domains have small-
982 world network structures and interfaces defined by expanded conformations. *Nat*
983 *Commun* **13**, 7722, doi:10.1038/s41467-022-35370-7 (2022).
984 50 Muhlberger, E., Weik, M., Volchkov, V. E., Klenk, H. D. & Becker, S. Comparison of the
985 transcription and replication strategies of marburg virus and Ebola virus by using artificial
986 replication systems. *J Virol* **73**, 2333-2342, doi:10.1128/JVI.73.3.2333-2342.1999 (1999).
987 51 Hoenen, T., Jung, S., Herwig, A., Groseth, A. & Becker, S. Both matrix proteins of Ebola
988 virus contribute to the regulation of viral genome replication and transcription. *Virology*
989 **403**, 56-66, doi:10.1016/j.virol.2010.04.002 (2010).
990 52 Halfmann, P. *et al.* Generation of biologically contained Ebola viruses. *Proc Natl Acad Sci*
991 *U S A* **105**, 1129-1133, doi:10.1073/pnas.0708057105 (2008).
992 53 Nanbo, A., Watanabe, S., Halfmann, P. & Kawaoka, Y. The spatio-temporal distribution
993 dynamics of Ebola virus proteins and RNA in infected cells. *Sci Rep* **3**, 1206,
994 doi:10.1038/srep01206 (2013).
995 54 Schudt, G. *et al.* Transport of Ebolavirus Nucleocapsids Is Dependent on Actin
996 Polymerization: Live-Cell Imaging Analysis of Ebolavirus-Infected Cells. *J Infect Dis* **212**
997 **Suppl 2**, S160-166, doi:10.1093/infdis/jiv083 (2015).
998 55 Bharat, T. A. *et al.* Structural dissection of Ebola virus and its assembly determinants using
999 cryo-electron tomography. *Proc Natl Acad Sci U S A* **109**, 4275-4280,
1000 doi:10.1073/pnas.1120453109 (2012).
1001 56 Takamatsu, Y., Kolesnikova, L. & Becker, S. Ebola virus proteins NP, VP35, and VP24 are
1002 essential and sufficient to mediate nucleocapsid transport. *Proc Natl Acad Sci U S A* **115**,
1003 1075-1080, doi:10.1073/pnas.1712263115 (2018).
1004 57 Mateo, M. *et al.* Knockdown of Ebola Virus VP24 Impairs Viral Nucleocapsid Assembly and
1005 Prevents Virus Replication. *The Journal of Infectious Diseases* **204**, S892-S896,
1006 doi:10.1093/infdis/jir311 (2011).
1007 58 Han, Y. *et al.* Directed Evolution of Split APEX2 Peroxidase. *ACS Chem Biol* **14**, 619-635,
1008 doi:10.1021/acschembio.8b00919 (2019).
1009 59 Wigglesworth, V. B. The use of osmium in the fixation and staining of tissues. *Proceedings*
1010 *of the Royal Society of London. Series B - Biological Sciences* **147**, 185-199,
1011 doi:10.1098/rspb.1957.0043 (1957).
1012 60 Neidle, S. & Stuart, D. I. The crystal and molecular structure of an osmium bispyridine
1013 adduct of thymine. *Biochim Biophys Acta* **418**, 226-231, doi:10.1016/0005-
1014 2787(76)90072-1 (1976).
1015 61 Zhang, J., Li, D., Zhang, J., Chen, D. & Murchie, A. I. Osmium tetroxide as a probe of RNA
1016 structure. *RNA* **23**, 483-492, doi:10.1261/rna.057539.116 (2017).
1017 62 Geisbert, T. W. & Jahrling, P. B. Differentiation of filoviruses by electron microscopy. *Virus*
1018 *Res* **39**, 129-150, doi:10.1016/0168-1702(95)00080-1 (1995).
1019 63 Beniac, D. R. *et al.* The organisation of Ebola virus reveals a capacity for extensive,
1020 modular polyploidy. *PLoS One* **7**, e29608, doi:10.1371/journal.pone.0029608 (2012).

1021 64 Watanabe, S., Noda, T., Halfmann, P., Jasenosky, L. & Kawaoka, Y. Ebola virus (EBOV) VP24
1022 inhibits transcription and replication of the EBOV genome. *J Infect Dis* **196 Suppl 2**, S284-
1023 290, doi:10.1086/520582 (2007).
1024 65 Watt, A. *et al.* A novel life cycle modeling system for Ebola virus shows a genome length-
1025 dependent role of VP24 in virus infectivity. *J Virol* **88**, 10511-10524,
1026 doi:10.1128/JVI.01272-14 (2014).
1027 66 Leung, D. W. *et al.* An Intrinsically Disordered Peptide from Ebola Virus VP35 Controls Viral
1028 RNA Synthesis by Modulating Nucleoprotein-RNA Interactions. *Cell Rep* **11**, 376-389,
1029 doi:10.1016/j.celrep.2015.03.034 (2015).
1030 67 Fix, J., Galloux, M., Blondot, M. L. & Eleouet, J. F. The insertion of fluorescent proteins in
1031 a variable region of respiratory syncytial virus L polymerase results in fluorescent and
1032 functional enzymes but with reduced activities. *Open Virol J* **5**, 103-108,
1033 doi:10.2174/1874357901105010103 (2011).
1034 68 Blanchard, E. L. *et al.* Polymerase-tagged respiratory syncytial virus reveals a dynamic
1035 rearrangement of the ribonucleocapsid complex during infection. *PLoS Pathog* **16**,
1036 e1008987, doi:10.1371/journal.ppat.1008987 (2020).
1037 69 Nilsson-Payant, B. E. *et al.* Reduced Nucleoprotein Availability Impairs Negative-Sense
1038 RNA Virus Replication and Promotes Host Recognition. *J Virol* **95**, doi:10.1128/JVI.02274-
1039 20 (2021).
1040 70 Hu, Z. *et al.* Inclusion bodies of human parainfluenza virus type 3 inhibit antiviral stress
1041 granule formation by shielding viral RNAs. *PLoS Pathog* **14**, e1006948,
1042 doi:10.1371/journal.ppat.1006948 (2018).
1043 71 Cahn, J. W. & Hilliard, J. E. Free Energy of a Nonuniform System. III. Nucleation in a Two-
1044 Component Incompressible Fluid. *The Journal of Chemical Physics* **31**, 688-699,
1045 doi:10.1063/1.1730447 (1959).
1046 72 Shimobayashi, S. F., Ronceray, P., Sanders, D. W., Haataja, M. P. & Brangwynne, C. P.
1047 Nucleation landscape of biomolecular condensates. *Nature* **599**, 503-506,
1048 doi:10.1038/s41586-021-03905-5 (2021).
1049 73 Ranganathan, S. & Shakhnovich, E. I. Dynamic metastable long-living droplets formed by
1050 sticker-spacer proteins. *eLife* **9**, e56159, doi:10.7554/eLife.56159 (2020).
1051 74 Tanaka, H. Viscoelastic phase separation in biological cells. *Communications Physics* **5**, 167,
1052 doi:10.1038/s42005-022-00947-7 (2022).
1053 75 Deflube, L. R. *et al.* Ebolavirus polymerase uses an unconventional genome replication
1054 mechanism. *Proc Natl Acad Sci U S A* **116**, 8535-8543, doi:10.1073/pnas.1815745116
1055 (2019).
1056 76 Griffin, B. A., Adams, S. R. & Tsien, R. Y. in *Site-Specific Protein Labeling: Methods and*
1057 *Protocols* (eds Arnaud Gautier & Marlon J. Hinner) 1-6 (Springer New York, 2015).
1058 77 Schindelin, J. *et al.* Fiji: an open-source platform for biological-image analysis. *Nat*
1059 *Methods* **9**, 676-682, doi:10.1038/nmeth.2019 (2012).
1060 78 Taylor, N. O., Wei, M.-T., Stone, H. A. & Brangwynne, C. P. Quantifying Dynamics in Phase-
1061 Separated Condensates Using Fluorescence Recovery after Photobleaching. *Biophysical*
1062 *Journal* **117**, 1285-1300, doi:https://doi.org/10.1016/j.bpj.2019.08.030 (2019).

1063 79 Fang, J. *et al.* Functional interactomes of the Ebola virus polymerase identified by
1064 proximity proteomics in the context of viral replication. *Cell Rep* **38**, 110544,
1065 doi:10.1016/j.celrep.2022.110544 (2022).
1066 80 Martell, J. D., Deerinck, T. J., Lam, S. S., Ellisman, M. H. & Ting, A. Y. Electron microscopy
1067 using the genetically encoded APEX2 tag in cultured mammalian cells. *Nat Protoc* **12**,
1068 1792-1816, doi:10.1038/nprot.2017.065 (2017).
1069 81 Phan, S. *et al.* 3D reconstruction of biological structures: automated procedures for
1070 alignment and reconstruction of multiple tilt series in electron tomography. *Adv Struct*
1071 *Chem Imaging* **2**, 8, doi:10.1186/s40679-016-0021-2 (2017).
1072